J. Fluid Mech. (1993), vol. 256, pp. 615–646

Vortex rings impinging on walls: axisymmetric and three-dimensional simulations

By PAOLO ORLANDI AND ROBERTO VERZICCO

Università di Roma "La Sapienza" Dipartimento di Meccanica e Aeronautica, via Eudossiana n° 18 00184, Roma, Italy

(Received 13 November 1992 and in revised form 3 May 1993)

Accurate numerical simulations of vortex rings impinging on flat boundaries revealed the same features observed in experiments. The results for the impact with a free-slip wall compared very well with previous numerical simulations that used spectral methods, and were also in qualitative agreement with experiments. The present simulation is mainly devoted to studying the more realistic case of rings interacting with a no-slip wall, experimentally studied by Walker *et al.* (1987). All the Reynolds numbers studied showed a very good agreement between experiments and simulations, and, at $Re_v > 1000$ the ejection of a new ring from the wall was seen. Axisymmetric simulations demonstrated that vortex pairing is the physical mechanism producing the ejection of the new ring. Three-dimensional simulations were also performed to investigate the effects of azimuthal instabilities. These simulations have confirmed that high-wavenumber instabilities originate in the compression phase of the secondary ring within the primary one. The large instability of the secondary ring has been explained by analysis of the rate-of-strain tensor and vorticity alignment. The differences between passive scalars and the vorticity field have been also investigated.

1. Introduction

In the last few years large efforts have been devoted to understanding the role of coherent structures in the generation of turbulence in wall-bounded flows. Jiménez & Moin (1991), who followed the evolution of a single coherent structure, observed that this structure was created by a previous one travelling near the wall with a small inclination. This picture agrees with the well-known observation that a vortex, coming close to a wall, generates opposite-sign vorticity that becomes unstable and is lifted from the wall. Viscous diffusion and vortex stretching are the driving mechanisms that generate complex interactions between primary and secondary vortices. A deeper understanding of the complex interaction of coherent structures with a wall can be gained by considering a single structure without streamwise motion, and letting it interact with a wall.

Robinson (1991) proposed that in wall-bounded flows there are different kinds of coherent structures: in the near-wall region there are isolated vortices of different shapes that tend to become round, while in the logarithmic region there are hairpin vortices aligned with the streamwise direction. A hairpin vortex can be thought of as the superimposition of a constant shear and a ring vortex. It can be considered a basic structure that, as it moves towards a wall, can approximately represent the bursting

process. Chu & Falco (1988), in an experimental study of boundary layers, observed rings moving towards the wall and producing, after the impact, complex vortical structures. The vortex ring, even with the simplified hypothesis of axisymmetry, allows for vortex stretching, the mechanism that produces the increase in vorticity in the wall region of a boundary layer. The other parts of a hairpin vortex are the legs, which can be approximated as two-dimensional vortices, on which vortex stretching does not act. In this case the interaction among the vortical structures depends substantially on the Reynolds number.

Previous two-dimensional calculations (Orlandi 1990) simulated the rebound of vortex dipoles from a wall for several Reynolds numbers in the range of $800 < Re_v < 3200$. At low Re most of the secondary vorticity was dissipated and two monopoles remained near the wall. At intermediate Reynolds numbers ($Re_v \approx 1600$), on the other hand, different patches of secondary vorticity merged and produced a new dipole of opposite-sign with enough circulation to migrate far from the wall. At higher Re complex interactions caused the formation of two tripolar structures that rotated near the wall. For the latter simulation an experimental confirmation was not found, but for the first two cases there was similarity with the experiments of vortex rings impinging on a solid wall by Walker *et al.* (1987, referred to as WSCD in the following), or of vortex rings impinging on a density interface by Dahm, Sheil & Tryggvason (1989), even if the two-dimensional calculations did not consider vortex stretching.

The purpose of the present study is to perform simulations of axisymmetric vortex rings approaching no-slip walls and to compare the results with the experimental observations by WSCD. A second goal is to understand whether the interaction differs from that of a vortex pair and whether the causes of the ejection are similar. WSCD observed for the first time the ejection of a new ring formed through interactions of new vorticity generated at the wall. The principal features of the entire process can be summarized as follows: at all the Reynolds numbers a thin vorticity layer is generated at the wall by induction of the primary ring; it rolls up and forms a secondary ring. Due to mutual induction these two rings move along a circular trajectory and the external ring penetrates into the interior of the primary ring. As Re increases, azimuthal vorticity kinks become visible and, only at high Re ($Re_v > 1000$), the ejection of the new vortex ring occurs. It could be argued that the azimuthal instabilities are the eventual cause of the ejection. However, also from flow visualizations, it seems that the pairing of secondary and tertiary vortices produces vortical structure with enough circulation to propel itself far from the wall.

Before performing full three-dimensional calculations, the axisymmetric simplification can help to verify whether the ejection of the new vortex ring is due to azimuthal instabilities or to vortex pairing. In the numerical simulation the vorticity field is calculated directly; thus, the vortex dynamics can be represented more clearly than in flow visualizations by dye. In the axisymmetric calculations the vorticity–streamfunction formulation has been used to reduce the CPU time, and consequently to allow very fine grids. This satisfies a twin purpose: to describe the generation and the evolution of the thin layer of wall vorticity at high Reynolds number, and to verify the grid independence of the solution. Calculations with grids up to 256×513 were used to simulate the range of Re_v considered in the WSCD experiment ($564 < Re_v < 3000$).

Numerical simulation of axisymmetric flows by spectral methods are very cumbersome, since they require special functions. They have been applied to free or colliding vortex rings (Stanaway 1988; Stanaway, Shariff & Hussain 1988); these solutions were compared with the present results. A finite difference scheme gives satisfactory results

when the discretization of the nonlinear terms fulfil global conservation properties (Arakawa 1966) and when stable and accurate time discretizations are used. The present numerical method is an extension of the two-dimensional method developed for the simulation of vortex dipoles impinging on flat and curved walls (Orlandi 1989*a*). The results for the collision of two vortex rings of the same strength compared very well with those of Stanaway (1988), which were in turn in good agreement with the experimental results of Kambe & Minota (1983). This collision is equivalent to the interaction of a vortex ring with a free-slip wall at very low Froude numbers. This case can be described by the Navier–Stokes equations within half a domain and a zero-vorticity assumption at the wall. As a further confirmation of the quality of the present numerical method it was observed that, after the collision, the shapes of the vortical structures compared well with those visualized by Bernal *et al.* (1989) in an experiment of vortex rings impinging on a clean free surface.

In the present study three-dimensional simulations are performed to understand the mechanism of the formation of azimuthal instabilities and to verify whether these instabilities influence the ejection velocity of the new ring. While for a free vortex ring there are theoretical (Widnall & Sullivan 1973), experimental (Sullivan, Widnall & Shaoul 1973) and numerical studies (Knio & Ghoniem 1990; Verzicco, Orlandi & Shariff 1992), the azimuthal instabilities of a ring impinging on a solid wall have been examined, to our knowledge, only in the experimental study by WSCD. The three-dimensional simulation of the Navier–Stokes equations in primitive variables confirmed that at $Re_v < 1000$ these instabilities did not grow, and that at $Re_v = 1250$, the largest growth in the secondary vortex is associated with its compression at the interior of the primary vortex. The grid independence of the results was checked by a grid refinement study; in three dimensions in the (r, z)-plane the grid was held equal to that reproducing the dynamics of the azimuthal vorticity satisfactorily in the axisymmetric case. The effects of a refinement in the azimuthal direction were analysed by comparing the results of the calculation in the whole domain with those of a calculation that used an equal number of points distributed in a domain of size $2\pi/n$, with n the wavenumber of the disturbance. In three dimensions the kinematics and dynamics of the vorticity components lead to a better understanding of the collision than can obtained from dye pictures. This important point has been confirmed by introducing passive scalars in the numerical experiment and by comparing their distribution with that of the azimuthal vorticity. Since the initial conditions for the markers were close to those in the experiments (although the Schmidt number in the simulation was smaller than in the experiment) the numerical results agreed well with the dye visualizations by WSCD. The simulation showed that an initial perturbation with a wavenumber $n = 5$ produced an energy growth smaller than that associated with $n = 10$. The energy associated with $n = 5$ was mainly confined within the primary while that corresponding to $n = 10$ was in the secondary ring. The numerical distributions of passive scalars and the dye visualizations by Cerra & Smith (1983) depicted the large deformations of the secondary ring as hairpin vortices. These vortices are responsible for the large growth of the $n = 10$ energy mode. Moreover, from the computed velocity field the eigenvalues, eigenvectors of the rate-of-strain tensor and their vorticity alignment were obtained. These quantities, together with the second and third invariants of the strain-rate tensor, show that the structure of the primary ring differs from that of the secondary. In the primary the vorticity is higher than the strain, making the primary more resistant to the external strain that drives the azimuthal instabilities. This explains why the azimuthal instabilities in the secondary grow faster than in the primary.

2. Equations and numerical scheme

2.1. *Axisymmetric case*

Numerical simulations of an axisymmetric vortex ring impinging on a wall must describe the most important events in the experiment of WSCD; that is, creation of thin vorticity layers at the wall and their roll-up. This new vortical structure, together with the primary ring, produces very intricate interactions of great interest at high *Re*. This process can be accurately represented only by fine grids. In axisymmetric calculations, the vorticity–streamfunction formulation fulfils the requirement of a reduction of memory and CPU time. The quantity $\hat{\omega} = \omega_\theta / r$, moreover, permits the nonlinear terms to be written in Jacobian $J(\hat{\omega}, \psi)$ form. In this form, there are discretized expressions (Arakawa 1966) conserving, in the limit for $\nu \to 0$, high-order invariants (kinetic energy and $\int \hat{\omega}^2$) and maintaining the skew symmetry of the Jacobian. We wish to emphasize that the fulfillment of global conservation properties avoids the generation of unphysical vortical structures.

WSCD found that accurate measurements of the circulation Γ are difficult, therefore they used the translation velocity and diameter of the ring to define the Reynolds number, $Re_v = V_0 d_0 / \nu$. In the present simulation t has been scaled by Γ / r_0^2 and ω_θ by r_0^2 / Γ; therefore, the Reynolds number is $Re_\Gamma = \Gamma / \nu$. The Navier–Stokes equations in vorticity–streamfunction formulation become

$$\left.\begin{aligned} \frac{\partial \omega_\theta}{\partial t} + J(\hat{\omega}, \psi) &= \frac{1}{Re}\left[\frac{\partial}{\partial r}\left(\frac{1}{r}\frac{\partial \omega_\theta r}{\partial r}\right) + \frac{\partial \omega_\theta}{\partial z^2}\right], \\ J(\hat{\omega}, \psi) &\equiv \frac{\partial \hat{\omega}}{\partial r}\frac{\partial \psi}{\partial x} - \frac{\partial \hat{\omega}}{\partial x}\frac{\partial \psi}{\partial r}. \end{aligned}\right\} \tag{2.1}$$

The streamfunction is related to the vorticity by

$$\omega_\theta = \frac{1}{r}\frac{\partial^2 \psi}{\partial z^2} + \frac{\partial}{\partial r}\left(\frac{1}{r}\frac{\partial \psi}{\partial r}\right), \tag{2.2}$$

and the velocities are related to the streamfunction by

$$v_z = -\frac{1}{r}\frac{\partial \psi}{\partial r}, \quad v_r = \frac{1}{r}\frac{\partial \psi}{\partial z}. \tag{2.3}$$

The Navier–Stokes equations are solved with the $\omega_\theta = 0$ symmetry condition at $r = 0$. The calculation of a vortex ring impinging on a wall could use non-uniform grids to extend the physical domain in the radial direction and to cluster the grid points near the wall and near the axis where the vorticity dynamics is concentrated. Coordinate transformations, however, usually reduce the spatial accuracy; for this reason we preferred to use a constant grid within a limited domain of size r_f in the radial direction and $z_f = 5r_0$ or less in the vertical direction. Vorticity and streamfunction boundary conditions are required at $r = r_f$. If $r_0(t = 0) \ll r_f$, with r_0 the toroidal radius of the ring, the assumption of $\omega_\theta = 0$ and $\psi = 0$ at $r = r_f$ is satisfactory. A more accurate condition, when $r_0(t = 0) < r_f$, is obtained by radiative boundary conditions (Orlanski 1976). With $r_f = 4r_0$ both assumptions have been used, without appreciable differences. Since radiative boundary conditions increase the CPU time, $\omega_\theta = 0$ and $\psi = 0$ have been assumed at $r = r_f$. For no-slip walls, boundary conditions are derived by differentiating the definition of vorticity

$$\omega_\theta = \left(\frac{\partial v_r}{\partial z} - \frac{\partial v_z}{\partial r}\right) \tag{2.4}$$

with respect to z, whereas for free-slip boundaries $\omega_\theta = 0$ holds. At $z = 0$ both, free-slip and no-slip boundary conditions have been used, while at $z = z_f$ a free-slip condition has been always assumed.

The numerical scheme slightly differs from the numerical scheme described in Orlandi (1989*a*), which we summarize shortly. The viscous terms are discretized by a centred second-order scheme and the advective terms by the Arakawa (1966) scheme. To avoid the viscous stability limitations, the viscous terms are implicit, and to save CPU time, as suggested by Briley & McDonald (1975), the resulting pentadiagonal matrix has been factored into two tridiagonal matrices. The solution of the first tridiagonal matrix requires boundary conditions for a pseudo-vorticity, that coincide with $\omega_\theta = 0$ when the radial sweep is performed before. By a sine FFT in the z-direction and a tridiagonal solver in the r-direction the streamfunction was calculated from (2.2). The boundary conditions at the solid wall produce an expression similar to that of Woods (1954), with second-order time accuracy when (2.1) is written in delta form. At high Re, an accurate wall vorticity is required to represent the vorticity generation, driving the successive evolution of the vortical structures.

A third-order Runge–Kutta scheme with two-level storage, explicit for the nonlinear terms and implicit for the viscous terms, has been used for time advancement. This scheme is the same as adopted by Rai & Moin (1991). Courant numbers larger than those permitted by the Adams–Bashforth scheme, allow a reduction of the CPU time required for the calculation. This scheme has the further advantage of using non-uniform time steps maintaining the second-order accuracy without introducing interpolation procedures.

2.2. *Three-dimensional case*

In the three-dimensional case the Navier–Stokes equations in primitive variables reduce the number of operations. In Cartesian (Harlow & Welch 1965) as well as in general curvilinear coordinates (Orlandi 1989*b*) it is convenient, in a finite difference scheme, to stagger the velocities and to locate the pressure at the centre of the cell. This choice gives the most compact form for the discrete *div* and *grad* operators and well-structured matrices leading to a solenoidal velocity within round-off errors. The continuity equation in cylindrical coordinates, with the quantities $q_\theta = v_\theta$, $q_r = rv_r$, $q_z = v_z$ takes a form similar to that in Cartesian coordinates

$$\frac{\partial q_r}{\partial r} + \frac{\partial q_\theta}{\partial \theta} + r\frac{\partial q_z}{\partial z} = 0. \tag{2.5}$$

These variables, moreover, simplify the treatment of the region around $r = 0$. The difficulties met in the discretization of the equations in this region, in our opinion, explain the few applications of finite difference schemes for the solution of the Navier–Stokes equations in cylindrical coordinates.

The momentum equations in terms of q_i are

$$\left.\begin{aligned}
\frac{Dq_\theta}{Dt} &= -\frac{1}{r}\frac{\partial p}{\partial \theta} + \frac{1}{Re}\left[\left(\frac{1}{r}\frac{\partial r q_\theta}{\partial r}\right) + \frac{1}{r^2}\frac{\partial^2 q_\theta}{\partial \theta^2} + \frac{\partial^2 q_\theta}{\partial z^2} + \frac{2}{r^3}\frac{\partial q_r}{\partial \theta}\right], \\
\frac{Dq_r}{Dt} &= -r\frac{\partial p}{\partial r} + \frac{1}{Re}\left[r\left(\frac{1}{r}\frac{\partial q_r}{\partial r}\right) + \frac{1}{r^2}\frac{\partial^2 q_r}{\partial \theta^2} + \frac{\partial^2 q_r}{\partial z^2} - \frac{2}{r}\frac{\partial q_\theta}{\partial \theta}\right], \\
\frac{Dq_z}{Dt} &= -\frac{\partial p}{\partial z} + \frac{1}{Re}\left[\frac{1}{r}\left(r\frac{\partial q_z}{\partial r}\right) + \frac{1}{r^2}\frac{\partial^2 q_z}{\partial \theta^2} + \frac{\partial^2 q_z}{\partial z^2}\right],
\end{aligned}\right\} \tag{2.6}$$

where

$$\left.\begin{aligned}
\frac{\mathrm{D}q_\theta}{\mathrm{D}t} &\equiv \frac{\partial q_\theta}{\partial t} + \frac{1}{r}\frac{\partial q_\theta q_r}{\partial r} + \frac{1}{r}\frac{\partial q_\theta^2}{\partial \theta} + \frac{\partial q_\theta q_z}{\partial z} + \frac{q_\theta q_r}{r^2}, \\
\frac{\mathrm{D}q_r}{\mathrm{D}t} &\equiv \frac{\partial q_r}{\partial t} + \frac{\partial}{\partial r}\left(\frac{q_r^2}{r}\right) + \frac{\partial}{\partial \theta}\left(\frac{q_\theta q_r}{r}\right) + \frac{\partial q_r q_z}{\partial z} - q_\theta^2, \\
\frac{\mathrm{D}q_z}{\mathrm{D}t} &\equiv \frac{\partial q_z}{\partial t} + \frac{1}{r}\frac{\partial q_r q_z}{\partial r} + \frac{1}{r}\frac{\partial q_\theta q_z}{\partial \theta} + \frac{\partial q_z^2}{\partial z}.
\end{aligned}\right\} \tag{2.7}$$

The equations, as in the axisymmetric case, have been made dimensionless using r_0/Γ as the velocity scale and $r_0^2/\rho\Gamma^2$ as the pressure scale. The previous considerations, concerning the computational domain and the use of uniform grids, hold in three dimensions. Free-slip conditions have been assumed at $r = r_f$ and at $z = z_f$, while at $z = 0$ the no-slip condition was imposed.

The numerical scheme, described by Verzicco & Orlandi (1992*a*), was validated by comparing the evolution of free rings without azimuthal disturbances with the results by the ω, ψ formulation. The conservation of impulse, circulation and moment of the impulse was checked, together with the free-slip assumption at $r = r_f$. The accuracy of the treatment of the region around $r, = 0$ was tested by the simulation of a tripole formation. The flow, in this case, developed in the (r, θ)-plane and the results were compared with those in Cartesian coordinates by Orlandi & van Heijst (1992). This is a meaningful test, since at $r = 0$, during the tripole formation the vorticity is large.

The numerical method has features in common with those in the vorticity stream–function formulation. Viscous and advective terms were discretized by centred second-order schemes. In three dimensions and in the limit of $\nu \to 0$, energy is conserved, and this holds for the discretized equations. The system of equations was solved by the fractional-step method (Rai & Moin 1991). The introduction of the pressure at the old time step in the non-solenoidal step simplifies the boundary conditions imposition. A scalar quantity Φ is introduced to project the non-solenoidal field onto a solenoidal one. The pressure is related to Φ, and Φ does not require explicit boundary conditions. The large-band matrix associated with the calculation of Φ is reduced to a tridiagonal matrix by a periodic FFT in the θ-direction and by a cosine FFT in z. This procedure is very efficient to get the solenoidal velocity field within round-off errors. The CPU time required to evaluate Φ is less than that necessary to evaluate the non-solenoidal field. The same third-order Runge–Kutta scheme mentioned previously was used to advance in time the non-solenoidal field; at each of the three sub-steps Φ is calculated.

In cylindrical coordinates at $r = 0$ the momentum equations are singular. The staggered variables locate q_θ at $i, j+\frac{1}{2}, k+\frac{1}{2}$, q_r at $i+\frac{1}{2}, j, k+\frac{1}{2}$ and q_z at $i+\frac{1}{2}, j+\frac{1}{2}, k$; then, for $j = 1$, only the q_r equation becomes singular. Since $q_r = 0$ at $r = 0$ the first radial point where q_r is evaluated is at $i+\frac{1}{2}, 2, k+\frac{1}{2}$, and here each term is discretized without any approximation. The second derivative in r at $i, \frac{3}{2}, k+\frac{1}{2}$ for q_θ has been expressed by the same approximations used by Rai & Moin (1991) in wall-bounded flows. The accuracy is reduced but, in the present case, since the velocity gradients close to the axis are smaller than those near a solid wall, this reduction of accuracy has a minor effect. q_z does not require any approximation on discretizing the equation at $i+\frac{1}{2}, \frac{3}{2}, k$.

3. Initial conditions

The Hill vortex is a spherical ring of radius a, with $\hat{\omega} = \text{const}$, for $r < a$ and $\hat{\omega} = 0$ elsewhere. This solution has been widely investigated since it satisfies the Euler equations. This vorticity distribution is appropriate for contour dynamics calculations (Shariff, Leonard & Ferziger 1989); however, due to the discontinuity at $r = a$, it is not appropriate for direct simulations. Stanaway *et al.* (1988) with a smoothing around $r = a$ did not obtain a distribution resembling that of the experiments. WSCD did not measure the initial vorticity distribution, and they assumed that the ring had the self-induced velocity (Lamb 1932)

$$V_0 = \frac{\Gamma}{4\pi r_0}\left[\log\left(\frac{8r_0}{a}\right) - 0.25\right], \tag{3.1}$$

valid for $a/r_0 \ll 1$. This type of vortex ring is known as a Kelvin–Hicks ring, with a core in a state of solid-body rotation and with a constant volume $r_0(t)a^2(t) = C$; as for the Hill vortex, finite differences do not represent accurately this discontinuous vorticity distribution. Based on these considerations, we decided to assign a Gaussian distribution as in other numerical simulations (Stanaway 1988; Stanaway, Shariff & Hussain 1988)

$$\left.\begin{aligned} \omega_\theta(t=0) &= \frac{\Gamma}{\pi a^2}\mathrm{e}^{-(s/a)^2}, \\ s^2 &\equiv (z-z_0)^2 + (r-r_0)^2, \end{aligned}\right\} \tag{3.2}$$

with r_0 and z_0 the centre of the ring core. For this distribution Saffman (1970) calculated the self-induced velocity; in the viscous case, to a good approximation, it is given by (3.1). This expression has been used to relate the Reynolds number Re_v as in WSCD to the present Re_Γ. With the value of the constant volume $C = 3.33 \times 10^{-2}\text{cm}^3$ and with $r_0 = 0.59$ cm for $a/r_0 = 0.4131$ it gives the scaling $Re_\Gamma = 2.316 Re_v$.

For most cases, the Gaussian ring has been initially located at a distance from the wall equal to twice the ring radius. A ring of opposite-sign vorticity was considered in the region at $r < 0$, in the axisymmetric case, to have zero vorticity at the centreline. The smoothed Hill's distribution was used to compare the results with those obtained in other simulations by spectral methods (Stanaway *et al.* 1988). In three dimensions an azimuthal disturbance was also introduced to study its evolution and growth after the wall interaction. The calculations were performed by imposing a radial displacement of the toroidal axis of the ring with an amplitude $\epsilon = 0.02$ and a wavenumber $n = 5$. Knio & Ghoneim (1990) used a similar perturbation in the numerical study of free evolving rings. In each vertical plane the streamfunction is calculated by (2.2) and q_r and q_z were obtained from the Stokes streamfunction; q_θ was derived from the continuity equation. This procedure does not yield zero axial vorticity, and it gives a large amount of energy in the $n = 5$ mode and a small amount in the $n = 10$ mode. This initial condition is appropriate for the purpose of investigating the energy growth in different modes. A random perturbation should give a condition closer to the experiments but, in this case, adequate resolution would require a large number of points in the azimuthal direction.

4. Results

4.1. *Free-slip wall*

This case has been considered for a close comparison with the results of spectral calculations and for a qualitative comparison with the flow visualizations by Bernal

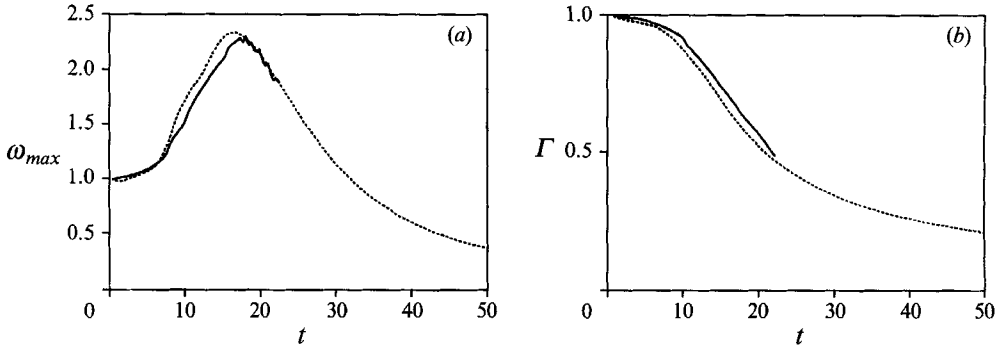

FIGURE 1. Time evolution of (*a*) peak vorticity and (*b*) circulation: ——, Stanaway *et al.* (1988); · · · ·, present.

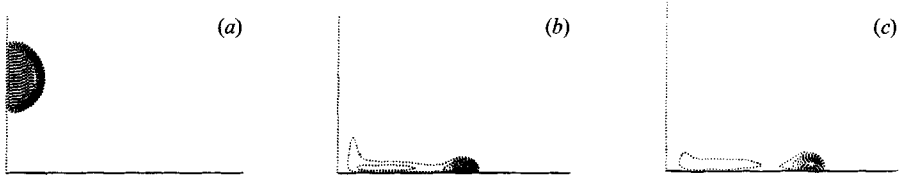

FIGURE 2. Vorticity contour plots of a Hill vortex colliding with a free-slip wall at $Re_\Gamma = 1073$: (*a*) $t = 0$, (*b*) $t = 40$, (*c*) $t = 50$. Contour increments are ± 0.07.

et al. (1989), who let rings interact with free surfaces with different amounts of surfactants. In pure water, the interaction is similar to the centred collision of two rings of the same strength. While an exact alignment between the two rings is difficult to reach in the experiment, the numerical simulation is simplified by the imposition of symmetry at the collision plane. Stanaway *et al.* (1988) considered two different rings: one is a thin -core ring with Gaussian distribution, and the other is a Hill vortex with smoothing to overcome the abrupt jump between vortical and irrotational regions. The initial vorticity distribution is

$$\omega = \frac{3}{2r}\sin\theta \begin{cases} 1, & r \leqslant r_i \\ 1 - f(\xi), & r_i \leqslant r < r_e \\ 0, & r_e < r, \end{cases} \tag{4.1}$$

where $f(\xi)$ is the smoothing function [$f(\xi) = 0$ for $r = r_i$ and $f(\xi) = 1$ for $r = r_e$] defined by Melander, McWilliams & Zabusky (1987), that connects the inner to the outer values of the vorticity. Stanaway *et al.* (1988) considered collisions at low and at high *Re*. At low *Re* ($Re_\Gamma = 300$) viscous dissipation overcomes the stretching effects; this, therefore, is not a satisfactory condition to test a numerical scheme designed to describe the evolution of the thin vorticity layers generated during the impact of a vortex with no-slip walls. At $Re_\Gamma = 1073$, on the other hand, vortex stretching produces a significant increase in the vorticity level, after the collision. Figure 1 shows the comparison between the present peak vorticity and circulation time history and the spectral results by Stanaway *et al.* (1988). The simulations, after the collision, show an increase in the peak vorticity. Vortex stretching causes this increase since, when the vortex comes close to its image vortex, its radius increases, and, to conserve $\hat{\omega} = \omega_\theta / r$, ω_θ must increase.

While two-dimensional calculations at high Reynolds numbers (Saffman 1979; Orlandi 1989*a*) do not show any substantial modification in the shape of the vortex

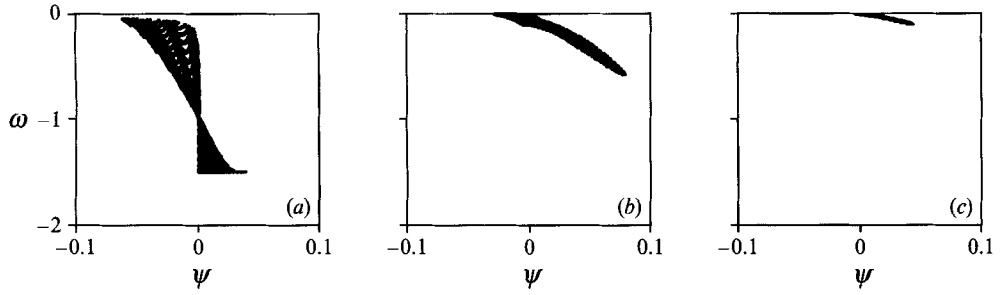

FIGURE 3. Vorticity *vs.* Stokes streamfunction scatter plots at the same times as figure 2.

after the wall collision, the axisymmetric simulation shows that the vortex has a head and an elongated tail (figure 2). The tail elongates and the head becomes smaller and, when the size of the head becomes sufficiently small, the peak vorticity is rapidly dissipated (figure 1*a*). The evolution of the circulation (figure 1*b*) during the approach of the vortex to the wall reveals that the diffusion of vorticity is negligible. After the collision, on the other hand, the gradients at the wall increase (figure 2) and the vorticity diffuses appreciably. During the formation of the head-tail structure (figure 2), the diffusion reaches a maximum and maintains this level for a short time. Later on ($t > 20$) the gradients at the wall decrease and the circulation diminishes at a lower rate. The tail is dissipated faster than the head since the vorticity intensity in the tail is smaller than that in the head.

We decided to run the simulation for a longer time than that of Stanaway *et al.* (1988), to investigate whether the small oscillations of the spectral calculation were physical or not. Simulations by grids up to 256×256 never showed any oscillations in time, and, therefore, we suppose that the oscillations in the spectral simulation have a numerical origin related to lack of grid resolution. Stanaway *et al.*, in fact, asserted that oscillations occurred in the tail region and that these were related to the small number of modes used (64×64). They furthermore pointed out that more accurate simulations require a memory larger than the in-core memory of a CRAY XMP48. In the present simulation, on the other hand, grid refinements are affordable since a 128×128 grid, which has twice the resolution of the spectral calculation, requires only 0.5 megawords of memory. While the present results predict a greater value of the peak vorticity, due to the lack of measurements in the experiment of Kambe & Minota (1983), it is difficult to establish which scheme is more reliable. It has, in any case, been shown that the present results are grid-independent, and we conclude that, at high *Re*, finite differences satisfying global conservation properties and using a stable time discretization give satisfactory results.

To confirm the accuracy of the present method, figure 2(*b*, *c*) shows that the shape of the vortex, in the first period after the collision, resembles very closely the visualizations by Bernal *et al.* (1989). In their experiment, however, at a later stage a secondary vortex ring was created far from the symmetry line. The formation of this secondary ring is a consequence of the surfactants found even on clean water, which change the surface tension and create interactions similar to those with a no-slip wall described in the following sub-section. The lack of detailed measurements by Bernal *et al.* (1989) does not allow a quantitative comparison with the present results.

A vortex ring impinging on a free-slip surface can be used to study the evolution of the functional relationship $\hat{\omega} = f(\psi)$ in a reference frame translating with the ring. A single-valued relationship is the steady solution of the inviscid vorticity

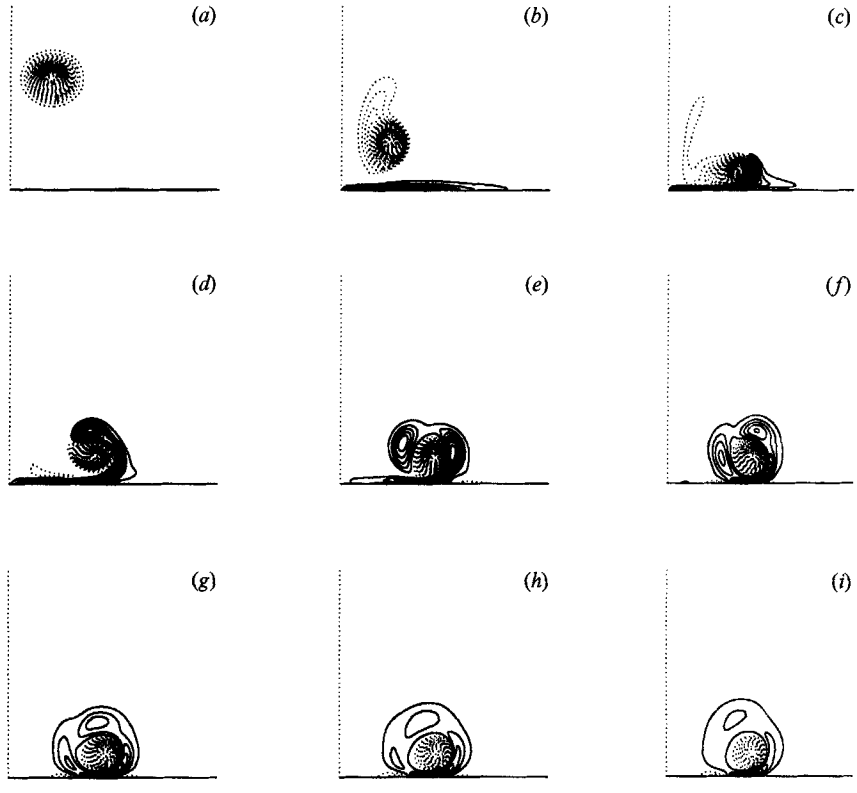

FIGURE 4. Vorticity contour plots at $Re_\Gamma = 1306$: (a) $t = 0$, (b) $t = 10$, (c) $t = 20$, (d) $t = 30$, (e) $t = 40$, (f) $t = 50$, (g) $t = 60$, (h) $t = 70$, (i) $t = 80$. Contour increments are ± 0.07, $\omega(t = 0)_{min} = -1.9$.

equation and $\hat{\omega} = \text{const}$, for $r < a$, is the simplest relationship possible, which is useful for theoretical considerations but is not suitable for numerical simulations. The smoothing function $f(\zeta)$ in (4.1) does not give a single-valued functional relationship $\hat{\omega} = f(\psi)$, as shown in figure 3(a). The calculation, at a very high Reynolds number ($Re = 10^4$), reduces the effect of diffusion; since the ring was located only a short distance from the wall, the time was not long enough to reach the equilibrium condition of $J(\hat{\omega}, \psi) \approx 0$ before the collision. Verzicco *et al.* (1992) performed this test for a free ring and they found that, at steady state, the functional relationship had an almost linear relationship with a steep slope. After the collision, the functional relationship becomes single-valued and linear, and figure 3(c) shows that it tends to the characteristic form of two-dimensional flows with a slope weaker than in the free ring. The tendency to the two-dimensional configuration is not surprising since, far from the axis, vortex stretching is not significant anymore in the ring. In this viscous calculation the linear relationship holds but, as far as the vorticity reduction is concerned, a true steady configuration is not achieved.

4.2. *No-slip wall, axisymmetric case*

The satisfactory results for a vortex ring colliding with a rigid free-slip wall encouraged us to simulate the impact with no-slip walls. In this case, the process consists of the generation of a very thin vorticity layer at the wall that rolls-up and forms a secondary vortex ring. The interaction between the rings is initially inviscid; later,

the interaction leads to different scenarios depending on *Re*. WSCD have visualized this mechanism; moreover, they attempted the explanation of the experimental observations by numerical methods based on viscous–inviscid interaction; this simplified model could fulfil its aim only partially. The full Navier–Stokes simulation, on the other hand, has the capability to describe the complex features of the phenomenon and to explain causes of events difficult to detect in the experiments. It is well know that the direct simulations are limited to small *Re*; however, the Reynolds number chosen in the present case is large enough to produce the growth of azimuthal disturbances, but small enough to be simulated by affordable grids. To describe this complex phenomenon the simulation requires the smallest grid-spacing compatible with the available computers, and a satisfactory three-dimensional grid refinement check is not possible. This test was, however, done in the axisymmetric case at the Reynolds number at which WSCD had observed the growth of azimuthal instabilities. The grid was then refined in the azimuthal direction as is described below.

WSCD reported the trajectories of the centre of each vortical structure together with several visualizations, making the comparison with the numerical simulations possible. The experiment is incomplete due to the unavailability of the vorticity distribution at $t = 0$; this fact could lead to the quantitative discrepancies between the present and the experimental trajectories. The trajectories of the peak vorticity have been compared with the experimental trajectories at $Re_v = 564, 1250, 1680$ and 2840 which correspond to $Re_\Gamma = 1306, 2895, 3890$ and 6577 respectively.

The interaction with a no-slip wall differs greatly from that with a free-slip wall; however, figure 4 shows that until $t = 10$ the thin wall layer does not affect the primary ring. It, therefore, does not differ from the shape it had in the free-slip collision or in the absence of walls. The thin wall layer is the boundary layer generated by the velocity field of the primary ring. Since there is an adverse pressure gradient, the boundary layer separates and, at the same time, the velocity field of the primary ring detaches it from the wall. The lifting of this positive layer stops the radial motion of the primary ring. At $t = 20$ the layer has significantly detached from the wall, which, in turn, induces a further thin layer of opposite-sign vorticity at the wall. WSCD observed the generation of the secondary layer, but the dye did not display the creation of the further thin layer. Although this layer does not affect the interaction of large-scale vortices, its appearance is a further proof that the numerical simulation can highlight structures not easily detected in the experiments.

The time history of the peak of primary and secondary vorticity (figure 5*a*), normalized by their initial values, show the increases in the primary ω_θ due to vortex stretching. The secondary vorticity reaches a value up two orders of magnitude greater than the maximum wall vorticity at $t = 0$. The negative vorticity concentrates in a thin layer, then it is rapidly dissipated as shown in figure 5(*a*). At $t \approx 25$ the circulation of the secondary vortex is almost the same than that of the primary (figure 5*b*); by considering that part of it is at the wall, it follows that primary and secondary rings form a dipolar structure moving along a circular trajectory. The new interaction with the wall causes the further bump at $t \approx 35$ (figure 5*a*). The trajectory of the centre of the primary ring (figure 6*b*) agrees with that by WSCD (figure 6*a*). Experimental and numerical observations show that the lift of the primary vortex by the secondary one causes a kink on the trajectory. At this *Re*, the primary vortex moves slowly to the right until the secondary layer stops the lateral translation characteristic in free-slip walls.

Since figure 4 is self-explanatory, it is not necessary to describe the vorticity dynamics in detail. However, we wish to point out that the primary ring remains near

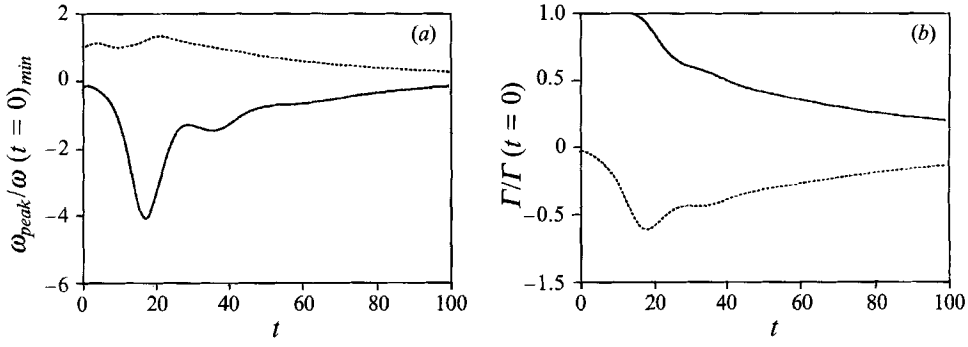

FIGURE 5. Time evolution at $Re_\Gamma = 1306$ of: (*a*) vorticity, (*b*) circulations.

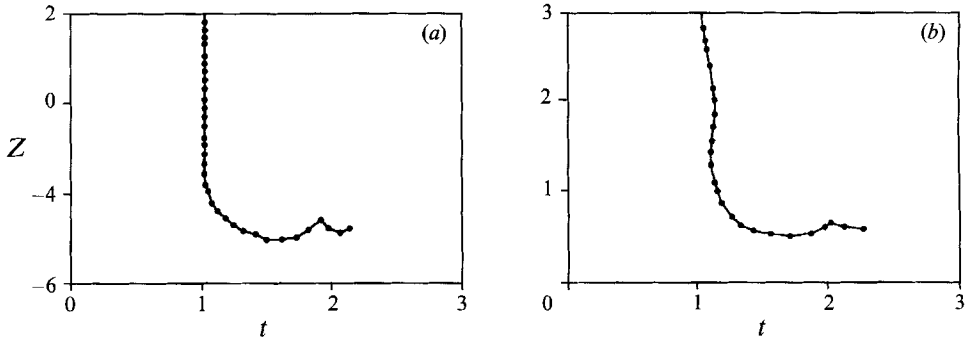

FIGURE 6. Trajectory of the centre of the primary ring at $Re_\Gamma = 1306$: (*a*) Experiment of WSCD, (*b*) present.

the wall, its initial strength is reduced, and it is encircled by secondary vorticity with high values at the wall. The two structures have an equal amount of positive and negative circulation (figure 5*b*). In the two-dimensional collision of a vortex dipole with a solid wall (Orlandi 1990), although the primary vorticity did not increase due to vortex stretching, the same qualitative behaviour was observed.

At $Re_\Gamma = 3890$, WSCD observed two loops in the trajectory of the primary vortex; figure 7 shows that the trajectory predicted by the numerical simulation (figure 7*b*) presents the same features observed in the experiment (figure 7*a*). The experiment shows that the two loops are similar, while the numerical simulation shows a second loop elongated towards the left. The difficulty of evaluating carefully the trajectories of the centre of the vortical structures in the experiment, and thus to detect the elongated second loop, is a possible explanation for this disagreement. This difficulty arises especially during the rebound, when the secondary structures can hide the primary ring (figure 26 in this paper and figure 12 in WSCD). Furthermore, viscous diffusion makes the detection at low *Re* more difficulty than at high *Re*, since at $Re = 6577$ both the experiment and the simulation predicted an elongated loop. The numerical simulation permits one to understand that the elongated loop is a consequence of the rise of the secondary structure that let the primary ring move towards the centreline. At this *Re*, secondary structures survive for a long time and cause the multiple rebound illustrated by the trajectory of the primary vortex.

The vorticity dynamics at $Re_\Gamma = 3890$ do not differ greatly from those at $Re_\Gamma = 2895$; thus, the features of the trajectory of the primary vortex in figure 7 can be explained by the vorticity contour plots at $Re_\Gamma = 2895$. At this *Re*, WSCD started

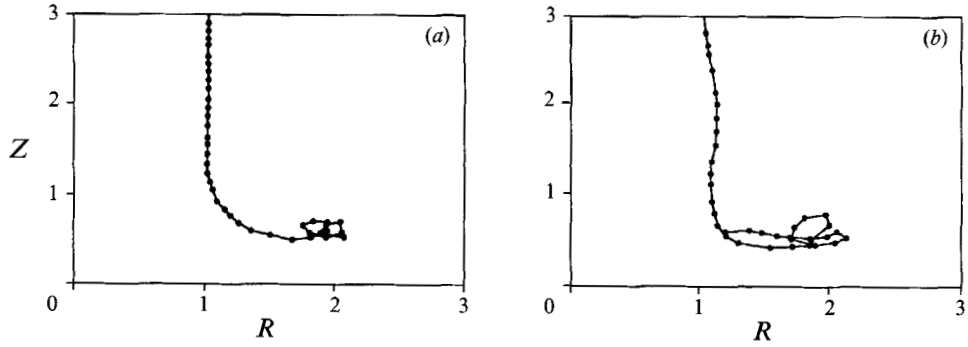

FIGURE 7. Trajectory of the centre of the primary ring at $Re_\Gamma = 2895$: (*a*) Experiment of WSCD, (*b*) present.

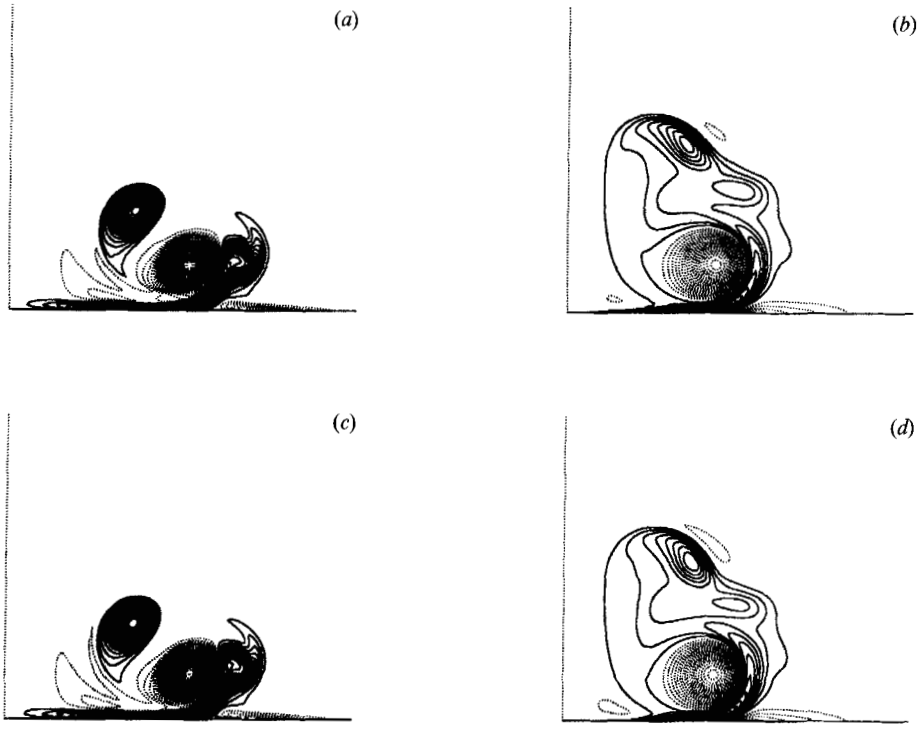

FIGURE 8. Vorticity contour plots at $Re_\Gamma = 2895$: (*a, b*) 128 × 128 grid at $t = 30$ and $t = 70$, (*c, d*) 256 × 512 grid, same times; contour increments are ±0.07

to observe azimuthal instabilities; therefore, we performed the three-dimensional simulations at this Reynolds number. The grid limitations in three dimensions suggested performing part of the grid refinement check in the (r, z)-plane. The aim was to prove that a 128 × 128 grid in a domain with radial extension $r_f = 4r_0$ and vertical extension $z_f = 3.5r_0$ is sufficient to capture the formation of secondary and tertiary vortices, and to describe the interactions among these structures. The grid refinement at this Reynolds number also proves that the direct simulation is adequate and that it is not necessary to use methods based on viscous–inviscid interactions (Peridier & Walker 1989). These methods require cumbersome programming efforts and the introduction of approximations makes the solution valid only for the first rebound

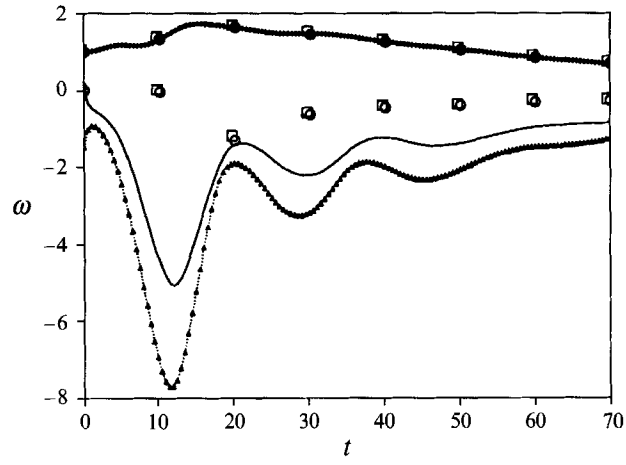

FIGURE 9. Time evolution of vorticity at $Re_\Gamma = 2895$: ——, positive 128 × 128 grid; - - -, negative 128 × 128; △, negative values 256 × 512; ◇, positive values 256 × 512. Peak values in the primary and secondary vortices indicated by symbols.

but not for the successive ones. This numerical technique could be appropriate at very high Reynolds numbers, where the direct simulation cannot be applied due to computer limitations. However at very high Re, as shown by the experiments, the incoming ring becomes turbulent and the viscous–inviscid interaction is even more difficult to compute. Figure 8, at $t = 30$ and at $t = 70$, shows vorticity contour plots obtained with the 128 × 128 (figure 8*a*, *b*) and the 256 × 512 (figure 8*c*, *d*) grids. Although there is a slight difference between the location of the vorticity peak in the coarse and fine grids, the formation of the large-scale vortex, at $t = 70$, by pairing of secondary and tertiary structures is predicted well. The time evolution of the peak vorticity (figure 9) shows similar trends for the two grids, with the same number of bumps for the secondary vorticity, each one representing the rebounds of the primary vortex. The differences in the minima can be explained by considering that the fine grid produces higher absolute values at the wall, but that these are concentrated in very thin regions and are also rapidly dissipated. The fast dissipation is confirmed by the steep increase of negative vorticity. Figure 9 shows that for the two grids the maxima almost coincide. Figure 8 and figure 9 together show that the two calculations differ only in the thin wall layers and the large scales do not differ in shape and strength. At times that are multiple of 10, the peak vorticity in the primary and in the secondary vortices has been calculated, confirming the grid independence of the large structures (figure 8).

This grid refinement encouraged us to perform three-dimensional simulations to study the more complex interaction of the structures and to investigate whether any difference in the ejection velocity of the new vortex ring occurred. Before analysing the full simulation, it is interesting to describe the Reynolds number dependence in axisymmetric calculations.

Figures 10 and 11 show the vorticity evolution, at $Re_\Gamma = 2895$ and $Re_\Gamma = 6577$, obtained on the same grid (256 × 512) in domains of different extension in the vertical direction. At $Re_\Gamma = 2895$ the height was fixed at $z_f = 3.5r_0$; this height was maintained in three dimensions because it gives sufficient resolution to resolve the small scales generated in the full simulation. At $Re_\Gamma = 6577$ the vertical size was increased up to $z_f = 5r_0$ to describe the stronger ring ejection. The two calculations, during the approach of the ring and immediately after the collision, show analogies

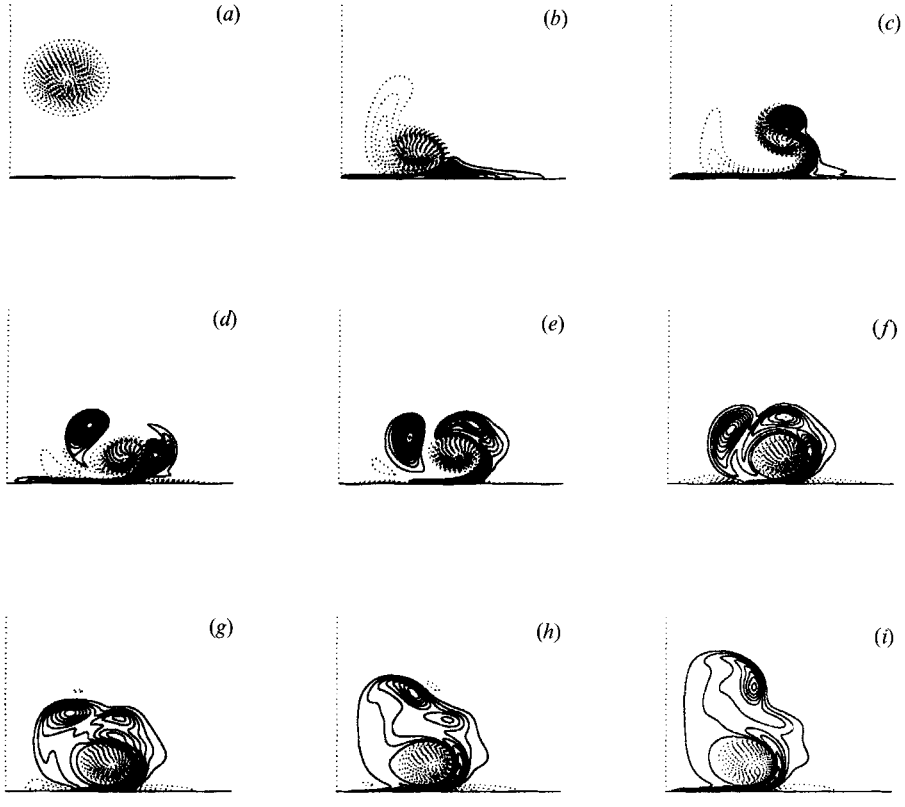

FIGURE 10. Vorticity contour plots at $Re_\Gamma = 2895$: (*a*) $t = 0$, (*b*) $t = 10$, (*c*) $t = 20$, (*d*) $t = 30$, (*e*) $t = 40$, (*f*) $t = 50$, (*g*) $t = 60$, (*h*) $t = 70$, (*i*) $t = 80$. Contour increments are ± 0.07, $\omega(t = 0)_{min} = -1.9$.

with figure 4. The reduced viscosity leads to secondary structures that break and form patches of vorticity with increasing circulation because of the merging process. The vortex merging, initiating at $t = 60$ (figure 10), allows us to give an explanation of the occurrence of the elongated loop in figure 7(*b*), since, due to the merging, vorticity disappears from the region close to the axis, letting the primary ring advect the secondary one. At $Re_\Gamma = 6577$, secondary and tertiary structures have higher vorticity levels that produce a very compact vortical structure, which continues to entrain tertiary vorticity; its circulation becomes so strong that fast ejection from the wall occurs.

This event is described by WSCD who evaluated the trajectories of the centres of the vortical structures. Figure 12(*a*, *b*) shows the good qualitative agreement between the trajectories of the numerical simulation (figure 12*b*) and experimental measurements (figure 12*a*). Both studies show the double loop of the primary vortex with the second loop elongated for the same reasons as previously described. The differences between the values in figure 12(*a*) and in figure 12(*b*), as already mentioned, could be ascribed to differences in vorticity distributions at $t = 0$. The shifting on the right, larger in the numerical simulation than in the experiment, could be tentatively explained by supposing that a flat vorticity distribution in the experiment produces interactions within a region of reduced size. This explanation could be verified through several simulations with different initial vorticity distributions, until a better agreement with the experiment is reached. The distribution of (3.2) however, captured the relevant features of the phenomenon, and so that tedious work is not necessary. Differences

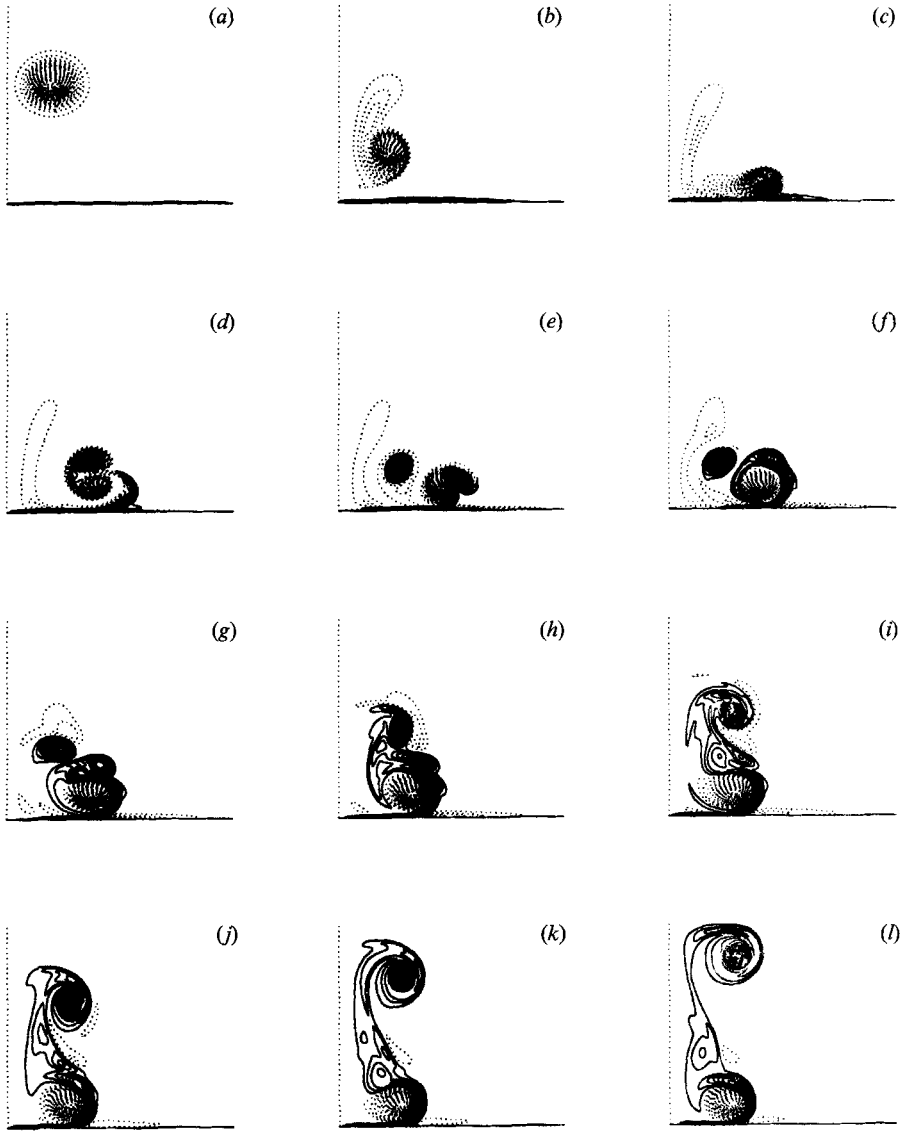

FIGURE 11. Vorticity contour plots at $Re_\Gamma = 6577$: (a) $t = 0$, (b) $t = 10$, (c) $t = 20$, (d) $t = 30$, (e) $t = 40$, (f) $t = 50$, (g) $t = 60$, (h) $t = 70$, (i) $t = 80$, (j) $t = 90$, (k) $t = 100$, (l) $t = 110$. Contour increments are ± 0.07, $\omega(t = 0)_{min} = -1.9$.

between the experiment and the numerical simulation could be also ascribed to three-dimensional effects. This is a further reason why the simulations of the full Navier–Stokes equations have been performed.

4.3. *No-slip wall, three-dimensional case*

In three dimensions a first calculation using a $65 \times 97 \times 128$ grid in $0 < \theta < 2\pi$, $0 < z < 4r_0$ and $0 < r < 4r_0$ has been performed, producing the time evolution of the two surface levels of azimuthal vorticity in figure 13. The perturbation with azimuthal wavenumber $n = 5$ modifies the initial shape of the ring but does not increase appreciably either during its descent towards the wall or during the first

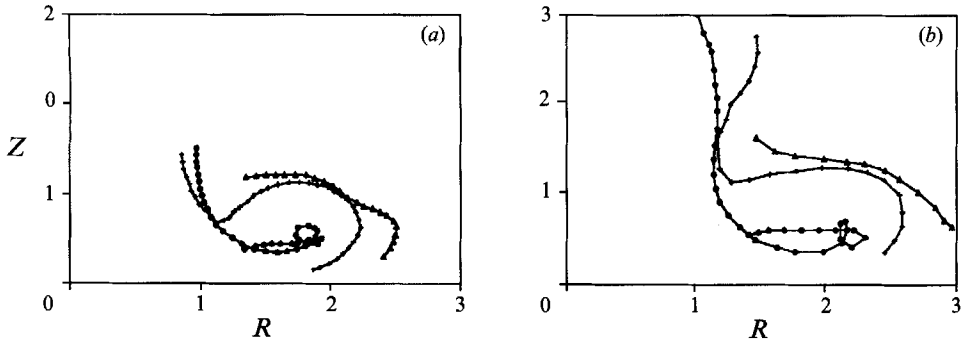

FIGURE 12. Trajectory of centres of primary (○), secondary (+) and tertiary (△) vortex rings. (*a*) Experiment of WSCD, (*b*) present at $Re_\Gamma = 6577$.

period of collision. At $t = 20$ the primary ring, in this perspective view partially covered by the secondary ring, does not present any substantial deformation. On the other hand, in the secondary ring, not only is the $n = 5$ perturbation present, but also the $n = 10$. The compression of the secondary ring, at the interior of the primary, produces an abrupt increase of the $n = 10$ wavenumber.

Between $t = 40$ and $t = 60$, the numerical simulation predicts, in the interior of the primary ring, the formation of vortical structures that resemble hairpin vortices, with the legs originating from the wall as in the experiment by Cerra & Smith (1983). After $t = 60$, figure 13(*g–i*) shows that the merging of secondary and tertiary rings, previously described in the axisymmetric case, leads to a very complex structure moving upwards.

Although the vorticity surfaces show distributions similar to the dye pictures of WSCD, we were not completely confident in the grid resolution. The flow symmetry is maintained in the whole domain ($0 < \theta < 2\pi$), as it is shown by the distributions of ω_θ and ω_z in an (r, θ)-plane passing through the centre of the primary vortex (figure 14). The figures at the top, through contour levels in the (r, z)-plane, indicate that azimuthal vorticity does not differ much from that in the axisymmetric case. The vertical vorticity, in the (r, z)- and in the (r, θ)-planes, shows that two rows of hairpin vortices form, the inner one with legs smaller than those in the outer circle. The two rows link each other as shown by the vertical cuts. From figure 14, and in particular from plots in the (r, θ)-plane, it appears that vortical structures of very small scale arise, and that the grid resolution of only 65 points in θ is not enough.

The same number of total grid points allows a more refined calculation using 128 points in r without decreasing r_f. Axisymmetric simulations showed that a reduction of the vertical size, at $Re_\Gamma = 2895$, is possible because of the limited upwards motion of the new structure. Then 128 points in z with $z_f = 3.5r_0$ produced the desired refinement. The highest refinement was obtained when 48 points were used in a domain $2\pi/5$ in the azimuthal direction; this is equivalent to using 240 points to represent the entire azimuthal span. Figure 15 shows a perspective view of the two surface vorticity levels, representing the primary (red), secondary and tertiary rings (green), for the refined calculation. Figure 13 and figure 15 show that, in the first stage of the collision, the results obtained on the two grids do not differ, but differences arise during the pairing at later times. An interesting outcome is the formation of hairpin vortices originating from the secondary ring. These vortices begin to appear at $t = 40$ and disappear during the pairing between secondary and tertiary rings. At the end of the pairing the new ring, which moves slowly away from the wall, has

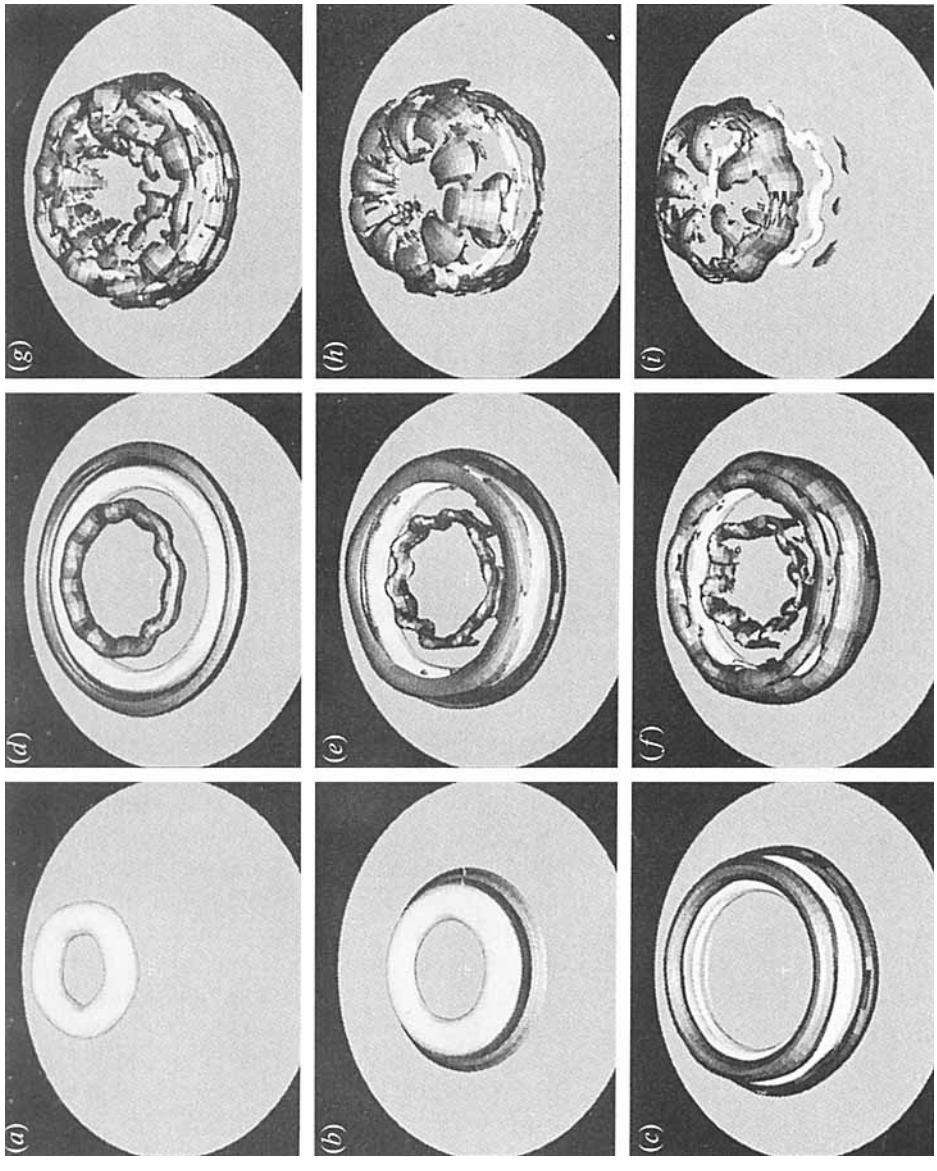

FIGURE 13. Azimuthal vorticity surfaces: $\omega_\theta = -1$ and $\omega_\theta = 0.5$. $Re_\Gamma = 2895$, grid $64 \times 96 \times 128$. (*a*) $t = 0$, (*b*) $t = 10$, (*c*) $t = 20$, (*d*) $t = 30$, (*e*) $t = 40$, (*f*) $t = 50$, (*g*) $t = 60$, (*h*) $t = 70$, (*i*) $t = 80$.

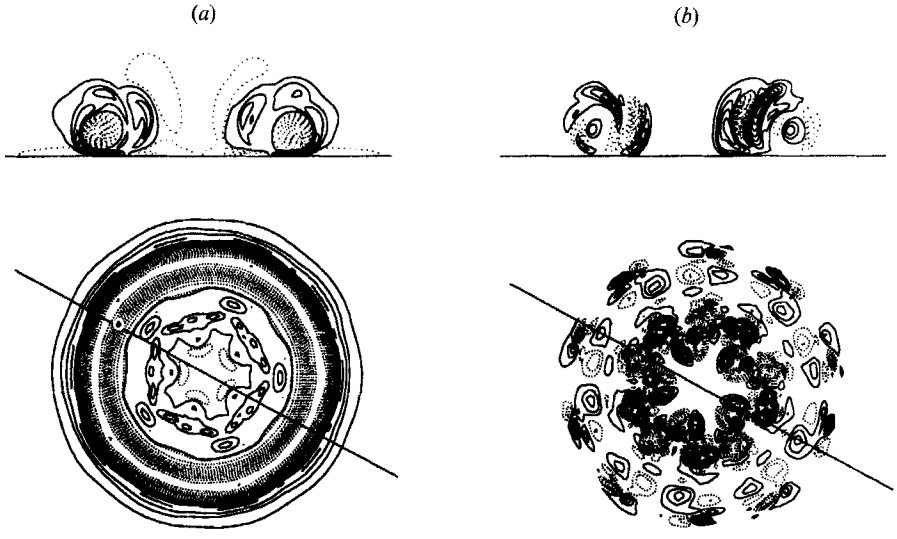

FIGURE 14. Contour plots of vorticity: (*a*) azimuthal ($\Delta\omega = \pm 0.2$), (*b*) vertical ($\Delta\omega = \pm 0.05$) at $t = 50$ and $Re_\Gamma = 2895$ using the coarse grid. Top: vertical sections. Bottom: plane sections at $z = 0.5$.

a well-defined, round shape. Moreover, at $t = 80$, all the vortical structures show a clear $n = 10$ instability.

Figures 16, 17 show the visualizations of ω_θ and ω_z on the fine grid at two different times. The analysis of the vorticity field at $t = 50$ clarifies the effect of the refinement, while that at $t = 30$ at two different horizontal planes leads to better understanding of the evolution of the structures. Figure 16(*a*) shows that in the secondary ring the $n = 10$ mode reached a sufficient amplitude to be clearly detected. A comparison between figure 13 and figure 15 shows that the amplitude of the deformation for the less resolved simulation is higher than that for the finer mesh. This implies that the inadequate resolution was causing injection of energy at high wavenumbers. This unphysical energy is more evident at $t = 50$, where a comparison between figure 14(*b*) and figure 17(*d*) shows that, far from the centre, the coarse grid produces regions with vorticity higher than that of the finer grid. The top figures in the two cases emphasize the hairpin vortex that, in the finer grid, has a more defined structure. At $t = 30$, figure 16(*b*) shows hairpin vortices that, although not visible in the perspective view in figure 15, appear in the visualization of figure 16. The hairpins at $t = 30$ (top of figure 16*b*), have a large head and small legs lying between the primary and the wall. The shape of the hairpins closely resembles the dye pictures in the experiment by Cerra & Smith (1983). At $t = 50$ the two rows of hairpins are still visible (figure 17) and they have a smoother shape than that yielded by the coarse grid. This comparison, however, also shows that the vorticity distribution is not altered drastically by the grid refinement, and we can argue that the calculation on the finer grid reached grid independence. The confidence in the results induced us to calculate the energy and to analyse the deformation tensor for a better understanding of the dynamics of the vortical structures.

Azimuthal FFTs of the velocities, followed by an integration of the energy in the (r, z)-plane, give the energy content at each wavenumber. The coarse grid simulation showed that all the modes smaller than $n = 5$ had a low energy content while only the modes that were multiples of $n = 5$ had a reasonable energy content. This is a

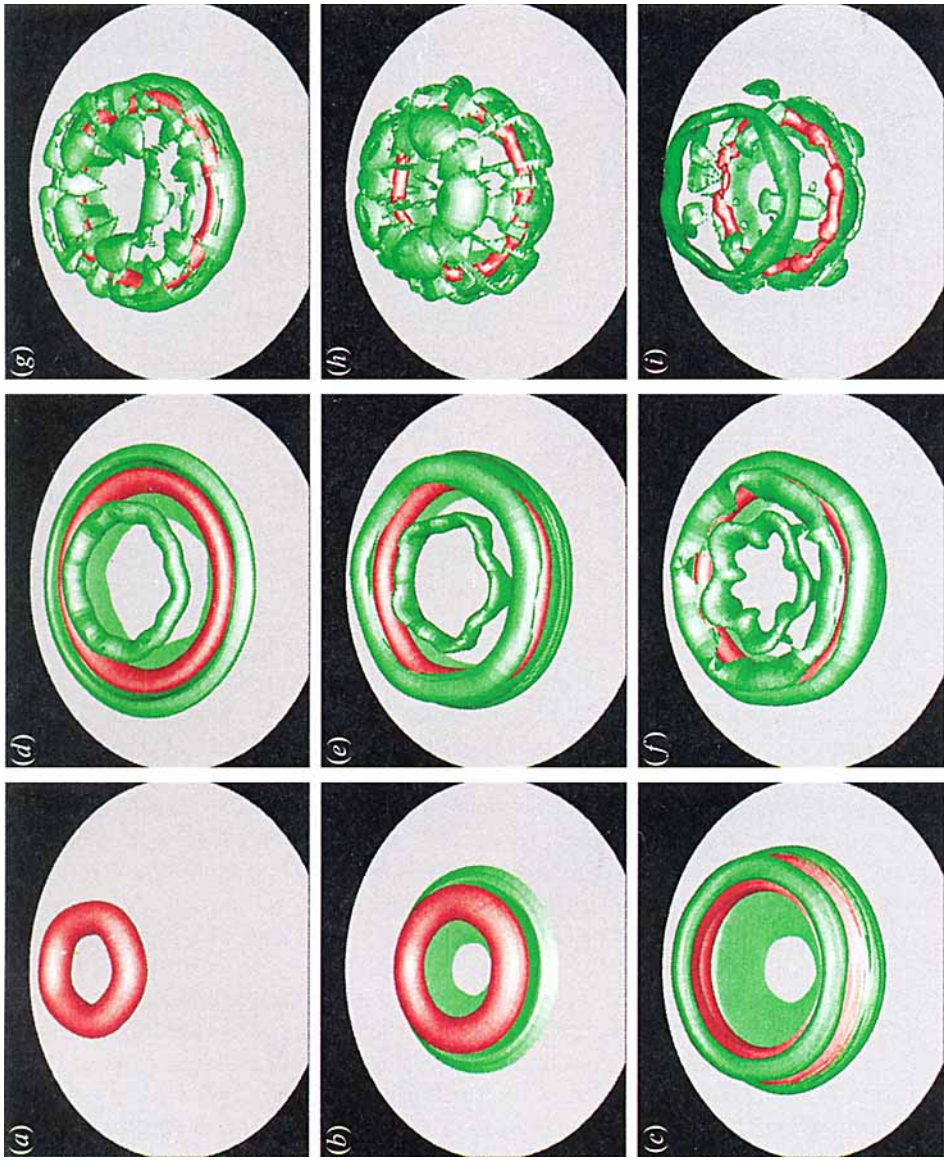

FIGURE 15. Azimuthal vorticity surfaces: $\omega_\theta = -1.0$ (red) and $\omega_\theta = 0.5$ (green). $Re_\tau = 2895$, grid $48 \times 128 \times 128$ ($2\pi/5$ in θ). (*a*) $t = 0$, (*b*) $t = 10$, (*c*) $t = 20$, (*d*) $t = 30$, (*e*) $t = 40$, (*f*) $t = 50$, (*g*) $t = 60$, (*h*) $t = 70$, (*i*) $t = 80$. The sequence in time is vertical from top-left to bottom-right.

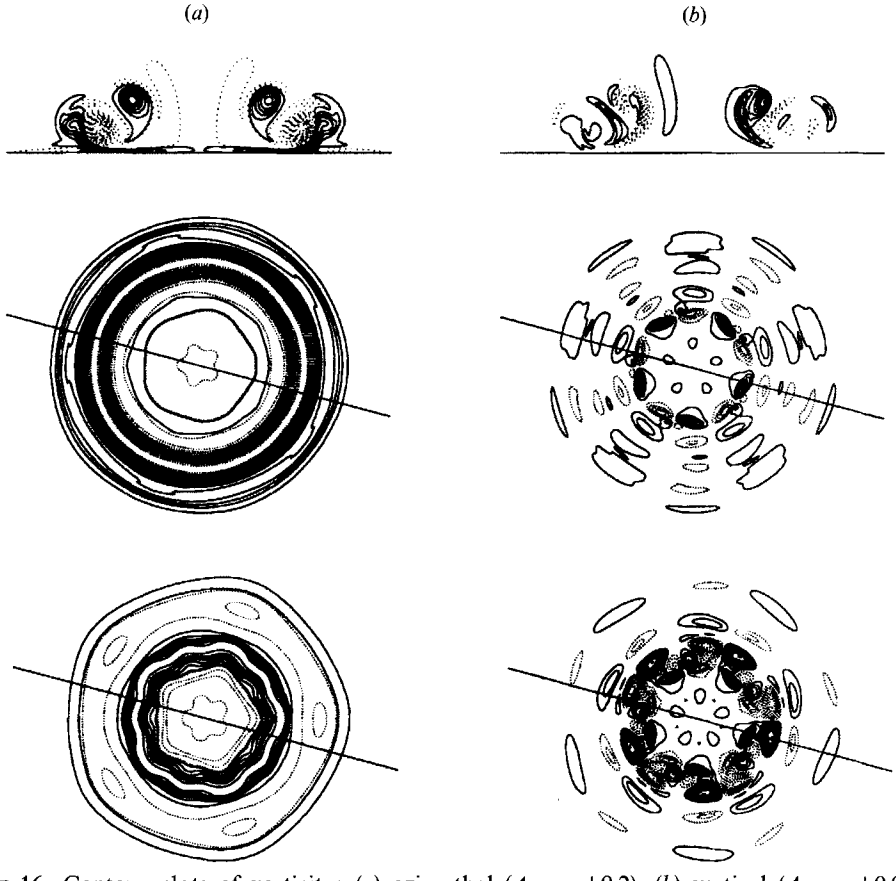

FIGURE 16. Contour plots of vorticity: (*a*) azimuthal ($\Delta\omega = \pm 0.2$), (*b*) vertical ($\Delta\omega = \pm 0.05$) at $t = 30$ and $Re_\Gamma = 2895$. Top: vertical sections. Centre: plane sections at $z = 0.5$. Bottom: plane sections at $z = 1$.

further proof that the calculation within 1/5th of the domain, producing only modes multiples of $n = 5$, is a good choice. Since the ring does not have any swirling motion, the simulation confirmed that the contributions to the kinetic energy come mainly from radial $[E_2(k)]$ and vertical $[E_3(k)]$ velocities. During the translation towards the wall the total energy in the zero wavenumber diminishes (figure 18*a*) and the decrease of the vertical velocity due to the effect of the wall produces most of the energy reduction. After the impact ($t > 10$), $E_3(k)$ reaches a level equal to that of $E_2(k)$ and both diminish because of viscous effects. The scales of these semi-log plots hide this energy decrease, which is, however, present. During the approach of the primary ring to the wall the $n = 5$ contribution to $E_3(k)$ decreases because of viscous effects, but later on, like the contribution to $E_2(k)$, it shows several peaks related to multiple rebounds. The imperfect assignment of the initial velocity field produced the low energy level ($O(10^{-9})$) in the $n = 10$ mode. This small amount increases significantly between $t = 15$ and $t = 20$. This change in slope coincides with the compression of the secondary in the interior of the primary ring. The energy content of the $n = 10$ mode, in the final period, becomes of the same order as that of $n = 5$. The total energy at each wavenumber, scaled by its initial amount (figure 18*d*), shows that the

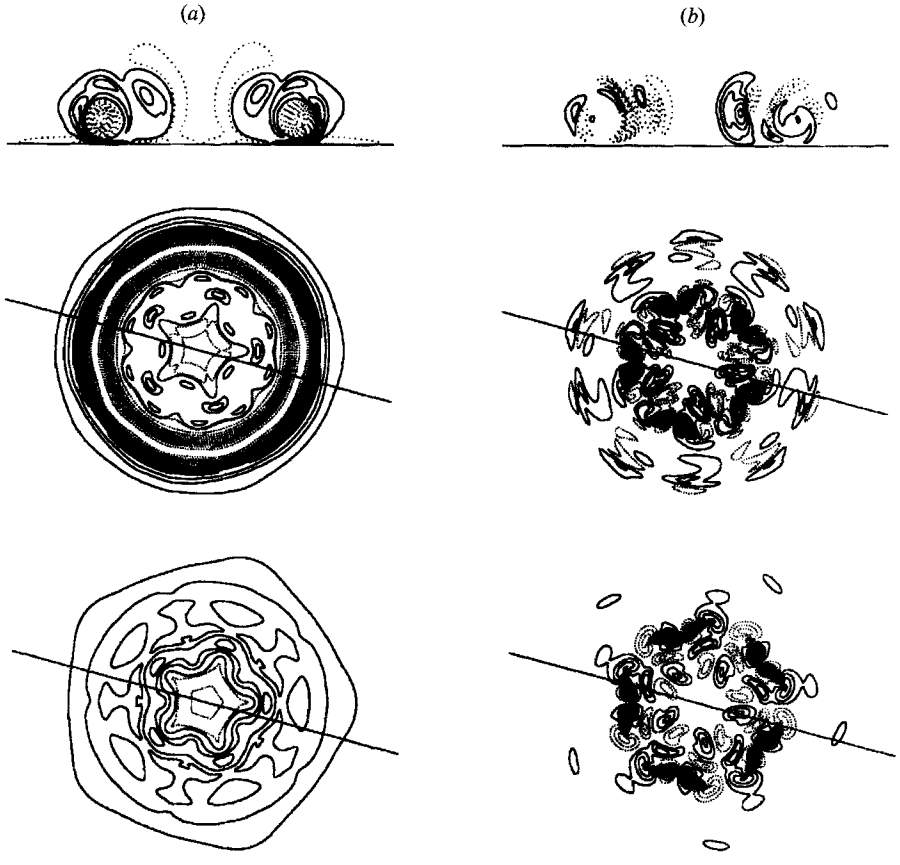

FIGURE 17. Contour plots of vorticity: (*a*) azimuthal ($\Delta\omega = \pm 0.2$), (*b*) vertical ($\Delta\omega = \pm 0.05$) at $t = 50$ and $Re_\Gamma = 2895$. Top: vertical sections. Centre: plane sections at $z = 0.5$. Bottom: plane sections at $z = 1$.

energy at $n = 10$ increases by four orders of magnitude and that the largest growth occurs during the compression of the secondary ring.

The energy was calculated without any discrimination between the energy in the primary and in the secondary rings. However, figures 16,17 had shown that the amplitudes of the azimuthal perturbations in the secondary are larger than in the primary. The evaluation of the invariants Q_S, R_S of the rate-of-strain tensor S_{ij} can clarify the causes of the difference between the primary and the secondary vortices. Furthermore, the alignment of the components of S_{ij} in the principal axes (α, β and γ) with the vorticity vector, and the probability distribution of the ratio between the largest strain and vorticity, indicate how stable a vorticity structure is. We performed the analysis at $t = 30$ and at $t = 50$ but we show the results only at $t = 50$, when in the secondary the hairpin vortices reached an appreciable deformation. The expressions for the rate-of-strain tensor in cylindrical coordinates, given by Orlandi & Verzicco (1993*a*), are not reported here. We recall that $i = 1 - 3$ respectively correspond to the θ-, r- and z-directions. The second (Q_S) and third (R_S) invariants are calculated in terms of α, β and γ as $Q_S = \alpha^2 + \beta^2 + \gamma^2$ and $R_S = \alpha\beta\gamma$. Q_S represents the magnitude of the rate-of-strain tensor; $R_S > 0$ indicates that two eigenvalues are negative and the vortex is rod-like, while a negative R_S represents a sheet-like vortex. For a better definition of the structure topology it is important to examine the ratio between the

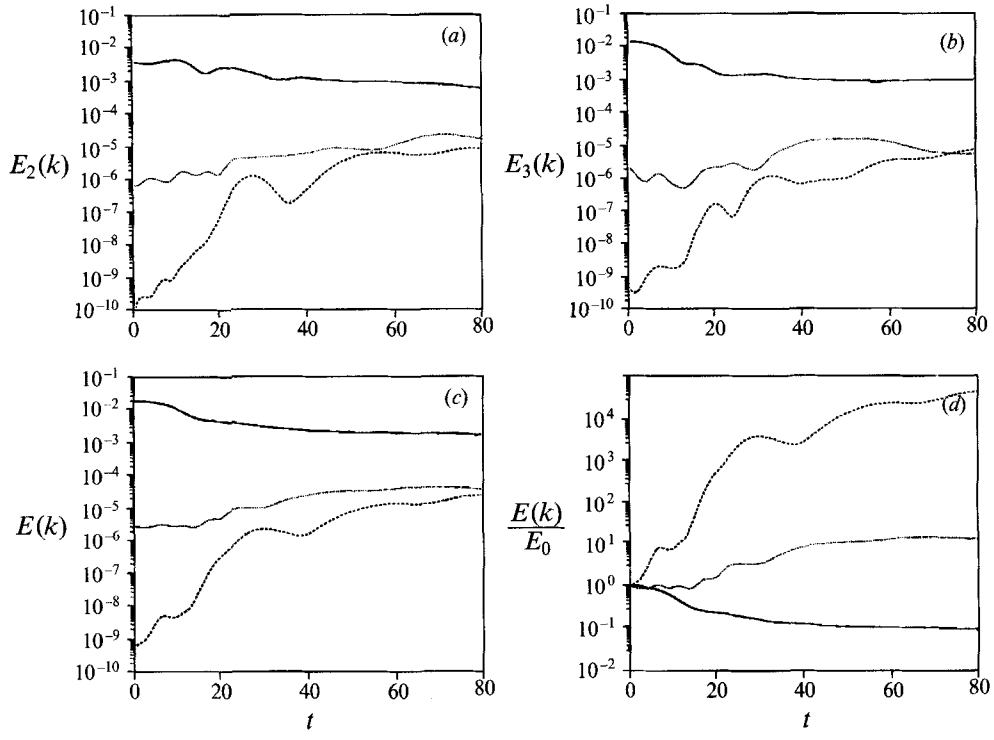

FIGURE 18. Time evolution of energy at wavenumbers $n = 0$ (——), $n = 5$ (· · · ·) and $n = 10$ (- - -): (*a*) radial, (*b*) vertical, (*c*) total, (*d*) total scaled by its initial value.

intermediate eigenvalue β and the positive one α. When there is a large number of points with $\beta \approx 0$, the structure is close to a two-dimensional vortex. Since we are interested in detecting well-deformed structure, we imposed a threshold of high probability of positive β, roughly $\beta/\alpha > 0.2$. In the calculation of these quantities the whole flow has been divided into two regions, one encircling the primary and the other including the secondary. This subdivision, which was accomplished by looking at the contour plots, is not exact; it was, however, found satisfactory for the present purposes. Within these regions, only the points where the vorticity magnitude $\omega_M = (\omega_i^2)^{\frac{1}{2}}$ exceeded a threshold level were considered; the threshold chosen was $\omega_M = 0.25$.

Results have shown that, within the primary ring, there are 10989 points where $R_S > 0$ and 10529 points where $R_S < 0$; within the secondary, on the other hand, R_S was positive at 13407 points and negative at 16740 points. It follows that in the primary ring there is almost the same number of round and flat eddies, indicating that the primary tends to be unstable. The primary, however, is more stable than the secondary, since in the latter there are more points with $R_S < 0$ than with $R_S > 0$. This consideration explains why the secondary ring, during its compression, is more unstable and why the deformations are larger than in the primary ring.

This remark is confirmed in figure 19(*a*, *b*) by scatter plots of $S_{ij}S_{ji}$ versus $-R_{ij}R_{ji}$. In cylindrical coordinates the invariant of the rate-of-rotation tensor R_{ij} is related to vorticity through $-R_{ij}R_{ji} = \omega_i^2/2 + (q_\theta/r)^2 - 2\omega_3 v_\theta/r$. Figure 19(*a*) shows that in the primary ring there is a large number of points with very strong vorticity and weak strain rate. In these regions the instabilities have a low growth rate. On the other

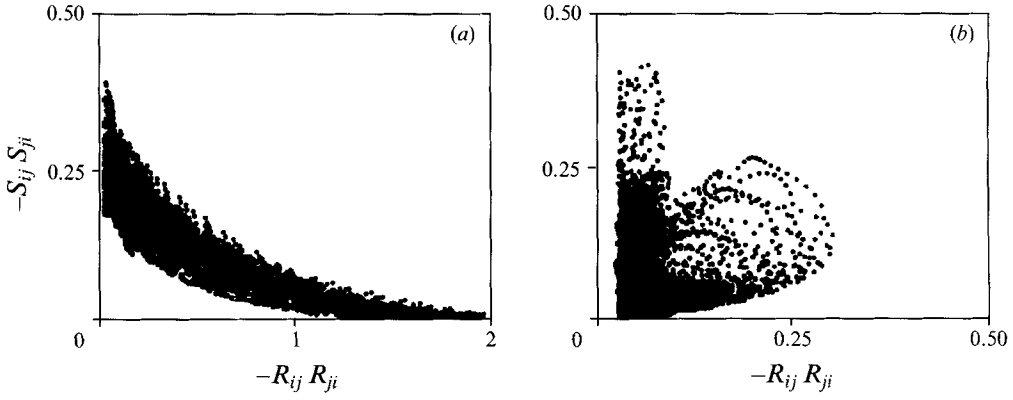

FIGURE 19. Scatter plots of $S_{ij}S_{ji}$ *vs*, $-R_{ij}R_{ji}$ at $t = 50$: (*a*) primary, (*b*) secondary.

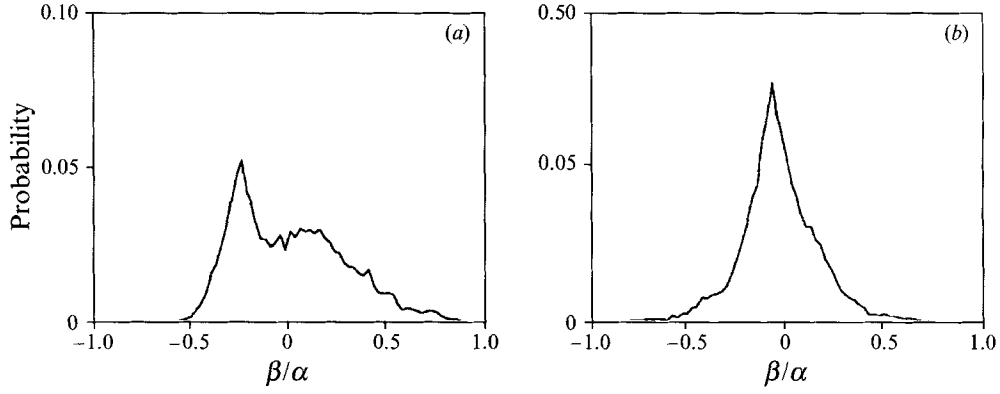

FIGURE 20. Probability distribution of ratio between intermediate and highest eigenvalues at $t = 50$: (*a*) primary, (*b*) secondary.

hand, in the secondary (figure 19*b*), although $S_{ij}S_{ji}$ does not change, the $-R_{ij}R_{ji}$ level is reduced, indicating that in these regions the Widnall instabilities grow.

The calculation of the eigenvalues of the strain-rate tensor was used by Ashurst *et al.* (1987) to characterize isotropic turbulence. They found that the shape of the tensor was $\alpha : \beta : \gamma = 3 : 1 : -4$, in agreement with the values by Jiménez (1992), who considered a large number of turbulent flows. In this case figure 20(*a*, *b*) shows that our results partly agree with those of isotropic turbulence. However, in this non-turbulent flow there is a large number of points where the intermediate strain is very small, a characteristic of axisymmetric flows. A comparison between the results in the two regions confirms that in the primary ring the probability of a rod-like structure is larger than in the secondary. Figure 20(*a*, *b*) shows that in both regions there is a low probability that $\beta/\alpha > 0.5$ and that the points where this occurs are those where well-defined sheet-like structures arise, making the growth of azimuthal instabilities possible.

The highest strain usually lies in planes normal to the direction of the strongest vorticity component, in this case the azimuthal direction. Figure 21(*a*) shows that in the primary α is lying in a plane normal to the azimuthal direction. In the axisymmetric case it is oriented at about 45° with the r- and z-directions, when the azimuthal deformation has reached a high level the positive strain has equal probability of being aligned with the radial or with the vertical directions. At $t = 30$,

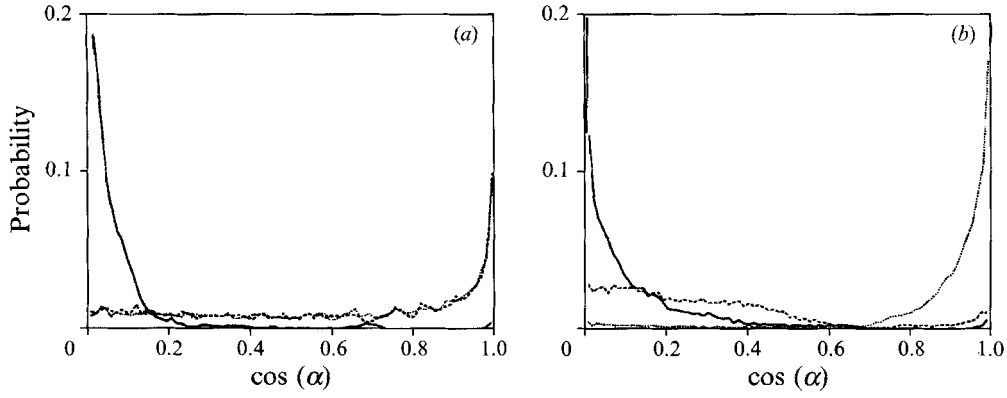

FIGURE 21. Probability distribution of the orientation of α at $t = 50$: ——, $S_{\alpha\theta}$; - - -, $S_{\alpha r}$; · · · ·, $S_{\alpha z}$. (*a*) Primary, (*b*) secondary.

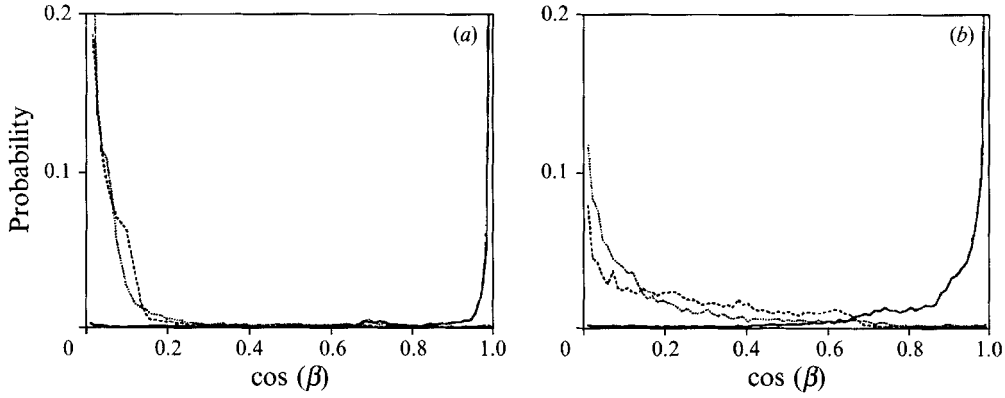

FIGURE 22. Probability distribution of the orientation of β at $t = 50$: ——, $S_{\beta\theta}$; - - -, $S_{\beta r}$; · · · ·, $S_{\beta z}$. (*a*) Primary, (*b*) secondary.

when the first rebound was completed there was a higher probability for α to be directed in the radial direction than in the vertical direction. The explanation is that, during the collision, the wall prevents the axial deformation and the primary is deformed mostly in the radial direction. Figure 22(*a*) shows the strong alignment of the intermediate strain in the azimuthal direction.

The projection of the vorticity vector on the principal axes shows that the vorticity mainly aligns with the intermediate strain (figure 23*a*), and at $t = 30$ this alignment was even better. This confirms that, at $t = 50$, the deformations of the primary ring do not grow because the secondary vorticity stops its motion. The same analysis, performed on the secondary ring, shows in figure 21(*b*) that the positive strain no longer lies in a plane normal to θ, and that it is oriented preferentially in the vertical direction. This proves that the secondary ring has the vertical deformation characteristic of a hairpin vortex. The intermediate strain (figure 22*b*) is still mainly oriented in the θ-direction, but not as much as in the primary ring. Figure 23(*b*) shows that in the secondary ring still there is a high probability of alignment with the intermediate strain but three-dimensional perturbations are more pronounced. The features derived from this analysis confirm the distribution of vorticity components in figure 16: in the primary ω_θ is predominant, while ω_z and ω_r are concentrated in the secondary. This is an explanation of the greater deformation of the secondary

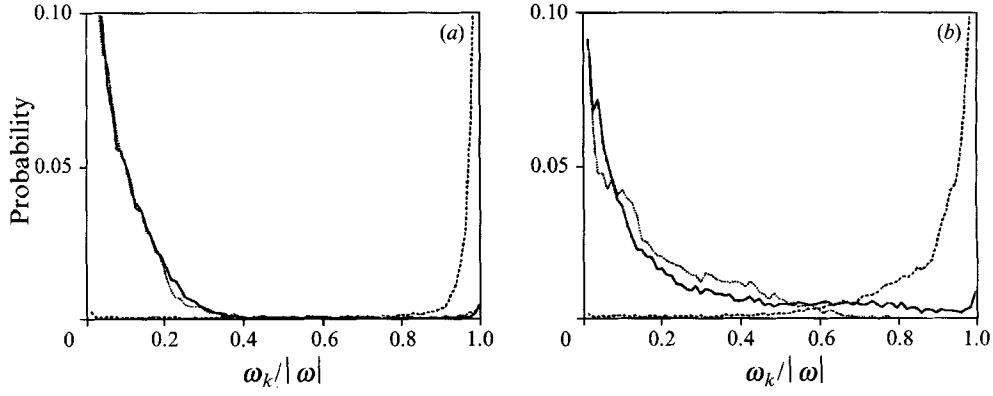

FIGURE 23. Probability distribution of vorticity components in the principal axes at $t = 50$: ——, $k = \alpha$; - - -, $k = \beta$; · · · ·, $k = \gamma$. (*a*) Primary ring, (*b*) secondary ring.

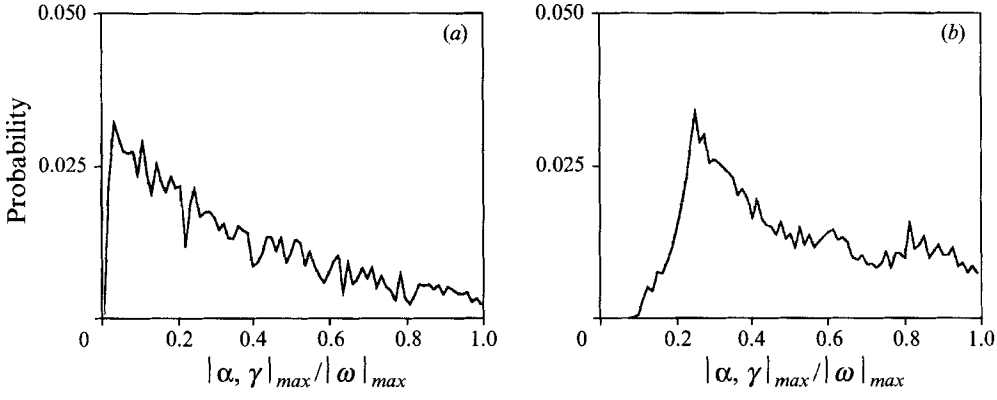

FIGURE 24. Probability distribution of the ratio between strain and vorticity at $t = 50$: (*a*) primary, (*b*) secondary.

than of the primary, and this statement is reinforced by figure 24(*a*, *b*), which show that the probability of finding a higher ratio between the maximum strain and the maximum vorticity in the secondary is larger than in the primary.

The purpose of the simulation was also to analyse whether azimuthal instabilities play a role in the ejection of the new ring. In figure 25, contour plots of azimuthal vorticity in the (r, z)-plane allow the results of the full simulation to be compared with those of the axisymmetric case. On the right side the section passes through a ω_z maximum, but on the left, through $\omega_z = 0$. Up to $t = 30$ there is no difference with the axisymmetric case of figure 10, but when ω_r and ω_z reached a high level (i.e. at $t = 30$, $\omega_z \approx \omega_r \approx 0.3$, $\omega_\theta \approx 2$), they contribute to produce ω_θ in regions where, in the axisymmetric case, it was missing. In fact between $t = 60$ and $t = 80$ the hairpin vortices contribute to produce ω_θ in the central region of the ring. A comparison between figure 25 and figure 10 shows that since the centre of the positive ω_θ is at a larger distance from the wall, in three dimensions the ejection velocity is greater than in the axisymmetric case.

To understand better whether flow visualizations by dye, similar to those in WSCD, can represent the vortical structures of rings colliding with solid walls, the calculation of passive scalars has been introduced in the full simulations. The equation for the concentration was discretized as those for the velocities, and finite differences

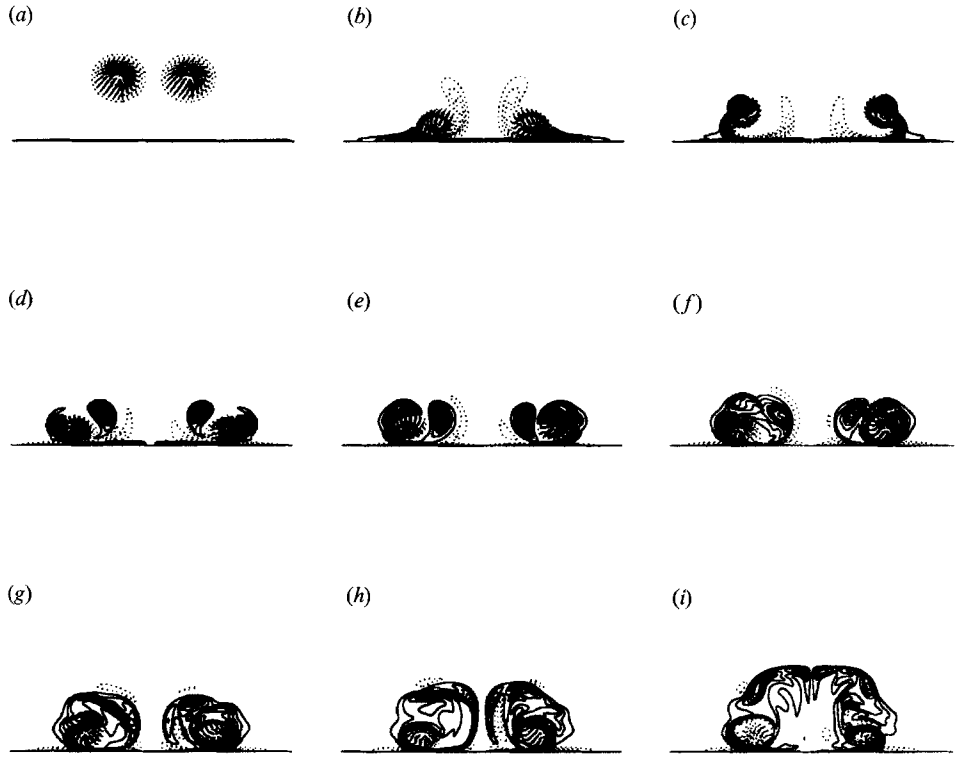

FIGURE 25. Azimuthal vorticity contour plots at $Re_\Gamma = 2895$: (*a*) $t = 0$, (*b*) $t = 10$, (*c*) $t = 20$, (*d*) $t = 30$, (*e*) $t = 40$, (*f*) $t = 50$, (g) $t = 60$, (*h*) $t = 70$, (*i*) $t = 80$. Contour increments are ± 0.07, $\omega(t = 0)_{min} = -1.9$.

were applied by locating the passive scalar at the centre of the cell. To be as close as possible to the dye visualizations in WSCD, the solution of two passive scalar equations has been performed. The first one had an initial Gaussian distribution equal to that for ω_θ in the primary ring. It reproduces the experimental condition with the dye introduced in the vortex-ring generator. The second equation had the concentration at $t = 0$ distributed in a thin layer near the wall, and it reproduces the experiment with dye placed on the wall. Figure 26 shows the evolution of two surface levels of the concentration fields marked with different colours. The simulation has been performed at $Sc = 1$, a value much smaller than that in the experiment, which was $O(10^3)$; this choice is dictated by the grid resolution. Despite this large difference in the Schmidt number, figure 26 is very similar to figures 15 and 16 in WSCD. A comparison between the passive scalar and the vorticity field shows that the former presents a smoother distribution than the latter; both, however, show the growth of the $n = 10$ wavenumber in the secondary. Differences arise in the long-term, for example at $t = 80$, where the dye does not accurately reproduce the effects of the pairing that generates the new ring-like structure. The most interesting outcome of this comparison is that the passive scalar is concentrated in regions of weak vorticity and is depleted in regions of intense vorticity. This behaviour confirms the results by Hussain & Melander (1991) in an axisymmetric simulation and by Orlandi & Verzicco (1993*b*) for a free vortex ring.

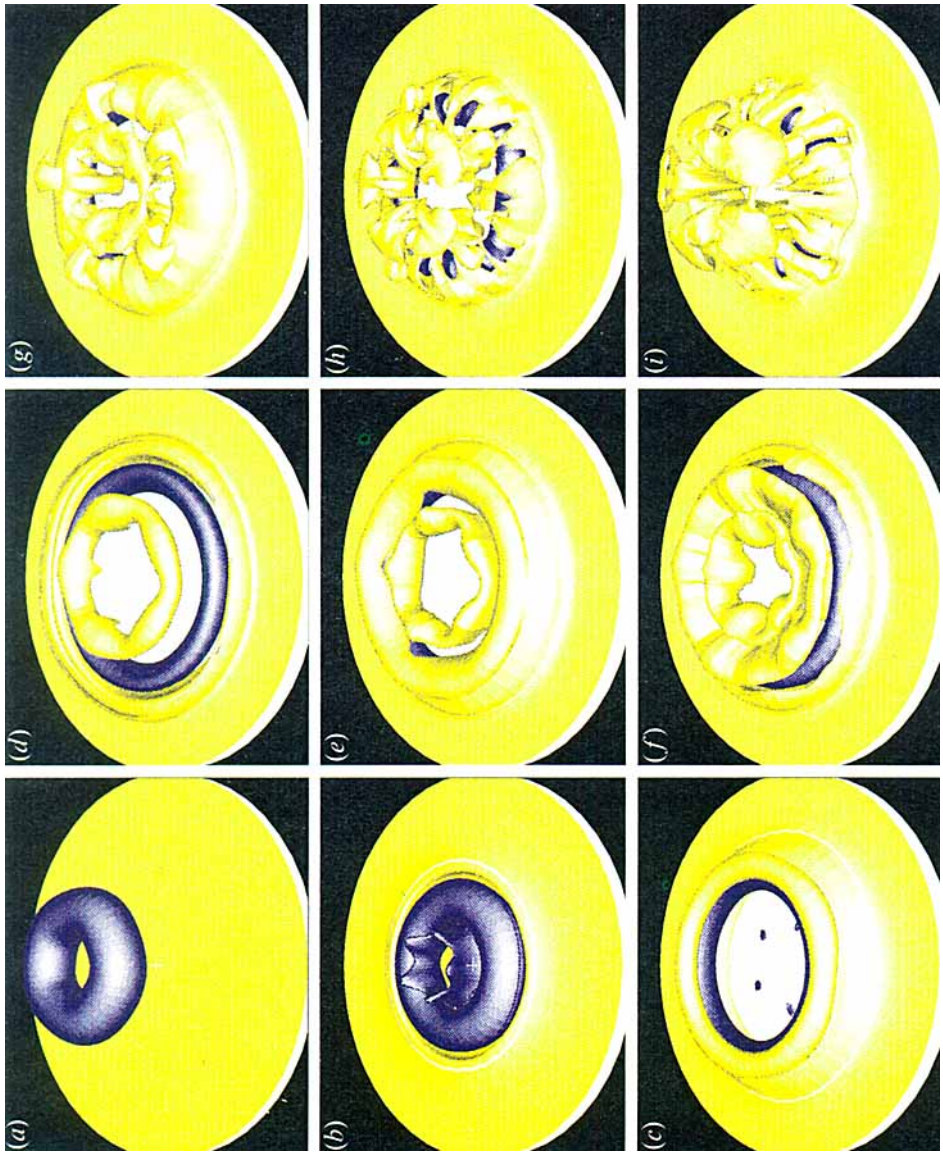

FIGURE 26. Passive scalar surfaces: $T = -0.4$ (blue) and $T = 0.2$ (yellow). $Re_\tau = 2895$, grid $48 \times 128 \times 128$ ($2\pi/5$ in θ). (*a*) $t = 0$, (*b*) $t = 10$, (*c*) $t = 20$, (*d*) $t = 30$, (*e*) $t = 40$, (*f*) $t = 50$, (*g*) $t = 60$, (*h*) $t = 70$, (*i*) $t = 80$. The sequence in time is vertical from top-left to bottom-right.

5. Conclusions

Numerical simulations of laminar vortex rings interacting with free-slip and no-slip walls have been carried out in the present study. The aim was to describe accurately the generation of secondary and tertiary vortical structures causing multiple rebounds of the primary ring. This paper does not focus on the mechanism creating the secondary structure at the wall, since WSCD described and explained it, and besides, this mechanism is similar to that studied for the first time by Harvey & Perry (1971) for a two-dimensional vortex approaching a wall.

Rather, this study has concentrated on the causes of the ejection of a new ring observed in the experiment by WSCD. In a previous two-dimensional simulation (Orlandi 1990) the ejection of a new dipolar structure was also observed; this paper aims to understand whether this ejection was different in the presence of vortex stretching. In both cases it has been shown that the merging of vortical structures leads to the formation of a new structure with sufficient circulation to move itself away from the wall. In two dimensions the new dipole forms very close to the centreline and it is generated only for $1000 < Re < 2000$. At $Re < 1000$, after multiple rebounds, two monopoles are formed that rotate near the wall. At $Re > 2000$ a new event takes place. It consists of the generation of two tripoles rotating near the wall. In the axisymmetric vortex ring the last event never occurs, and differences in the location of merging with the two-dimensional case arise. After the first rebound, the secondary structure remains in a more elevated position where it merges with the tertiary vortex continuously generated at the wall. At low Re, the viscosity reduces the circulation and the vortices do not move away from the wall. At a higher Re, the circulation can grow and it reaches a sufficient value to detach the new ring from the wall region. In the range of Re considered by WSCD, the trajectories of the vortices in the axisymmetric case agree qualitatively with those in the experiment. From this set of axisymmetric simulations, we concluded that the mechanism producing a new structure with enough circulation to propel itself far from the wall is the vortex pairing, as in two dimensions. Vortex stretching produces some differences in the position where the pairing occurs. From the simulations as well as from the experiments it appears that the first stage of the impact does not depend greatly on Re, and that the primary and the secondary rings interact in an inviscid manner. The effect of Re is important in the second stage, when the merging depends on the amount of circulation they have achieved. In the numerical simulation, the mechanism of pairing has been understood by the analysis of the vorticity field.

The full simulation requires a resolution sufficient to describe the interactions of elongated structures in the vertical direction with a core size smaller than the core of the primary ring. It showed that the interaction does not differ substantially from that in the axisymmetric case. At least at $Re_\Gamma = 2895$, in three dimensions, the ejection velocity of the new ring is only slightly higher than in the axisymmetric case. The full simulation, both through the vorticity field and passive scalars, revealed the same features as the flow visualization. In the first stage a thin vorticity sheet of opposite-sign is generated at the wall; this layer rolls up and forms, together with the primary ring, a pair moving on a circular trajectory. The secondary ring, while being compressed in the interior of the primary ring, shows the growth of azimuthal instabilities. In laboratory experiments the natural perturbation causes an instability with a wavenumber $n = 10$. In the numerical simulation an $n = 5$ perturbation has been assigned at $t = 0$, and the inaccuracy of initial conditions also produced a much smaller perturbation with $n = 10$. Using surfaces of vorticity and passive scalar it was

shown that during the compression the $n = 10$ mode grew much faster than the $n = 5$ in the secondary ring, in agreement with the experimental findings of WSCD. In the primary ring, on the other hand, the $n = 5$ perturbation grew in the initial stage, and, only in the final stage, did the $n = 10$ mode reach a substantial magnitude. The numerical simulation also predicted, in agreement with experiment (Cerra & Smith 1983), that, in the secondary ring, hairpin vortices are formed in the central region.

In the experiments it is difficult to understand why in the intermediate period the primary behaves differently from the secondary ring. Moreover a theoretical analysis, similar to that introduced by Widnall & Sullivan (1973), is difficult because of the complexity of the flow field. The numerical simulation data allowed better understanding of these differences, through the calculation of the eigenvalues and eigenvectors of the rate-of-strain tensor. These quantities emphasized that in the primary and in secondary rings the strain level is almost equal in magnitude, but in the former there is a large number of points where the vorticity overcomes the strain field. This explains the higher resistance of the primary to azimuthal perturbations. The opposite occurs in the secondary, which is more unstable. Furthermore, the calculation of the intermediate eigenvalue revealed that in the primary there are more points with two negative eigenvalues, which represents rod-like vortices that are more stable than sheet-like vortices.

We conclude that this direct simulation was useful to verify the interesting features of the collision of vortex rings with a solid wall, for the first time observed in the experiment of WSCD. Following the trend in the last few years, the data bases from the simulation, once validated with accurate experiments, bring a better understanding of the physics of complex flows. In this case light was shed on the differences between primary and secondary rings. A deeper understanding of the vorticity dynamics can be also obtained by the analysis of the contribution of each term in the vorticity transport equations, and this will be the topic of a forthcoming study.

The authors wish to thank Dr K. Shariff for the very fruitful discussions during his visit to Rome. The suggestion of one of the referees to perform the simulation of passive scalars is also acknowledged. The research was supported by a grant from "Ministero dell' Università e della Ricerca Scientifica", MURST MPI 40%.

REFERENCES

ARAKAWA, A. 1966 Computational design for long term numerical integration of the equations of fluid motion: Two-dimensional incompressible flow. Part I. *J. Comp. Phys.* **1**, 119–143.

ASHURST, W. T., KERSTEIN, A. R., KERR, R. M. & GIBSON, C. H. 1987 Alignment of vorticity and scalar gradient with strain rate in simulated Navier-Stokes turbulence. *Phys. Fluids* **30**, 2343–2353.

BERNAL, L. P., HIRSA, A., KWON, J. T. & WILLMARTH W. W. 1989 On the interaction of vortex rings and pairs with a free surface for varying amounts of surface active agent. *Phys. Fluids* A **1**, 2001–2004.

BRILEY, W. R. & MCDONALD, H. 1975 Solution of three-dimensional compressible Navier-Stokes equations by an implicit technique. *Proc. Fourth Intl. Conf. on Numerical Methods in Fluid Dynamics*. Lecture Notes in Physics, vol 35, p. 105. Springer.

CERRA, A. W. & SMITH, C. R. 1983 Experimental observations of vortex ring interaction adjacent to a surface. *Report FM-4 Department of Mechanical Engineering and Mechanics Lehigh University, Bethlehem.*

CHU, C. C & FALCO, R. E. 1988 Vortex ring/viscous wall layer interaction model of the turbulence production process near walls. *Exp. Fluids* **6**, 305–325.

DAHM, W. J. A., SHEIL, C. M. & TRYGGVASON, G. 1989 Dynamics of vortex interaction with a density interface. *J. Fluid Mech.* **205**, 1–43.

HARLOW, F. H. & WELCH, J. E. 1965 Numerical calculation of time-dependent viscous incompressible flow of fluid with free surface. *Phys. Fluids* **8**, 2182–2189.

HARVEY, J. K. & PERRY, F. J. 1971 Flowfield produced by trailing vortices in the vicinity of the ground. *AIAA J.* **9**, 1659–1661.

HUSSAIN, F. & MELANDER, M. V. 1991 Understanding turbulence via vortex dynamics. In *Studies in Turbulence*, pp. 157–178. Springer.

JIMÉNEZ, J. 1992 Kinematic alignment effects in turbulent flows. *Phys. Fluids* A **4**, 652–654.

JIMÉNEZ, J. & MOIN, P. 1991 The minimal flow unit in near wall turbulence. *J. Fluid Mech.* **225**, 213–241.

KAMBE, T. & MINOTA, T. 1983 Acoustic wave radiated by head-on collision of two vortex rings. *Proc. R. Soc. Lond.* A **386**, 277–308.

KNIO, O. M. & GHONIEM, O. M. 1990 Numerical study of three-dimensional vortex method. *J. Comp. Phys.* **86**, 75–106.

LAMB, H. 1932 *Hydrodynamics.* Cambridge University Press.

MELANDER, M. V., MCWILLIAMS, J. C. & ZABUSKY, N. J. 1987 Axisymmetrization and vorticity gradient intensification of an isolated two-dimensional vortex through filamentation. *J. Fluid Mech.* **178**, 137–159.

ORLANDI, P. 1989*a* Numerical simulation of vortices motion in presence of solid boundaries. *Proc. 8th GAMM on Numerical Methods in Fluid Mechanics* (ed. P. Wesseling), pp. 436–441. Vieweg.

ORLANDI, P. 1989*b* A numerical method for direct simulation of turbulence in complex geometries. *Center for Turbulence Research, Annual Research Briefs 1989*, pp. 215–222.

ORLANDI, P. 1990 Vortex dipole rebound from a wall. *Phys. Fluids* A **2**, 1429–1436.

ORLANDI, P. & HEIJST, G. J. F. VAN 1992 Numerical simulation of tripolar vortices in 2D flow. *Fluid Dyn. Res.* **9**, 179–206.

ORLANDI, P. & VERZICCO, R. 1993*a* Identification of zones in a free evolving vortex ring. *Appl. Sci. Res.* (to appear); also *Proc. IUTAM Symp. on Eddy Structure Identification in Free Turbulent Shear Flows, Poitiers.*

ORLANDI, P. & VERZICCO, R. 1993*b* Free vortex rings, analogies and differences between vorticity and a passive scalar. *Proc. NATO Adv. Res. Group (Grenoble 1992).*

ORLANSKI, I. 1976 A simple boundary condition for unbounded hyperbolic flows. *J. Comp. Phys.* **21**, 251–269.

PERIDIER, V. J. & WALKER, J. D. A. 1989 Vortex-induced boundary-layer separation. *Report FM-13 Department of Mechanical Engineering and Mechanics Lehigh University, Bethlehem.*

RAI, M. M. & MOIN, P. 1991 Direct simulations of turbulent flow using finite-difference schemes. *J. Comp. Phys.* **96**, 15–53.

ROBINSON, S. K. 1991 Coherent motions in the turbulent boundary layer. *Ann. Rev. Fluid Mech.* **23**, 601–639.

SAFFMAN, P. G. 1970 The velocity of viscous vortex rings. *Stud. Appl. Math.* **49**, 371–379.

SAFFMAN, P. G. 1979 The approach of a vortex pair to a plane surface. *J. Fluid Mech.* **92**, 497–503.

SHARIFF, K., LEONARD, A. & FERZIGER, J. H. 1989 Dynamics of a class of vortex rings. *NASA TM* 102257.

STANAWAY, S. 1988 A numerical study of viscous vortex rings using a spectral method. PhD Thesis, Aeronautics and Astronautics Dept., Stanford University. Also *NASA TM* 101041.

STANAWAY, S. SHARIFF, K. & HUSSAIN, F. 1988 Head-on collision of viscous vortex rings. *Proc. CTR Summer School 1988.*

SULLIVAN, J. P., WIDNALL, S. E. & SHAOUL, E. 1973 Study of vortex rings using a laser Doppler velocimeter. *AIAA J.* **11**, 1384–1389.

VERZICCO, R. & ORLANDI, P. 1992 A finite difference scheme for direct simulation in cylindrical coordinates *Presented at the ICOSAHOM 92, Montpelier*; also *J. Comp. Phys.* (Submitted.)

VERZICCO, R., ORLANDI, P. & SHARIFF, K. R. 1992 A numerical simulation of three-dimensional vortex rings instabilities. *J. Fluid Mech.* (To be submitted).

WALKER, J. D. A., SMITH, C. R., CERRA, A. W. & DOLIGASKI, J. L. 1987 The impact of a vortex ring on a wall. *J. Fluid Mech.* **181**, 99–140 (referred to herein as WSCD).

WIDNALL, S. E. & SULLIVAN, J. P. 1973 On the stability of vortex rings. *Proc. R. Soc. Lond.* A **332**, 335–353.

WOODS, L. C. 1954 A note on the numerical solution of fourth order differential equations. *Aero. Q.* **5**, 176–184.